Second-order nonlinear analysis of instability in three-layer nanoscale composite planar liquid sheets

Xiaocong Yang and Wentong Qiao
School of Astronautics, Beihang University, Beijng 100191, China

Hui Deng, Qingchang Meng, and Bingrui Xu*
Department of Basic Courses, Naval University of Engineering, Wuhan 430033, China

Qingfei Fu†
School of Astronautics, Beihang University, Beijng 100191, China
and Ningbo Institute of Technology, Beihang University, Ningbo 315100, China

(Received 2 November 2023; accepted 26 November 2024; published 26 December 2024)

The thermal drawing method has been widely used in fiber fabrication with thickness down to the microscopic scale, where the flow instability plays an important role in obtaining nanowires or many intriguing patterns. Inspired by this, we performed an exploratory second-order nonlinear analysis to investigate the nonlinear instabilities of a planar liquid sheet under dual mode. The dispersion relations of two modes and the formula for surface waves were obtained. Analysis indicates that van der Waals forces promote perturbation development, and the varicose mode dominates the development of surface waves. As the surface wave evolves, second-order perturbations gradually become dominant, and a portion of the first-order perturbations transfers to the second order takes on a dominant role. The nonlinearity introduced by the second-order perturbations in the development of surface waves has been analytically resolved, which can provide an explanation for the formation of the main and satellite liquid filaments after the rupture of the liquid sheet. Additionally, the application of the theoretical findings in nanowire manufacturing was investigated. Nanowire diameter prediction revealed its dependence on the liquid sheet thickness, with the main filament-to-satellite-filaments diameter ratio ranging 1.91–1.94. The ratio can be modified by adjusting the perturbation amplitude, which influences the diameter ratio positively. The impact of arbitrary microperturbations was also explored, showing negligible effects within the effective wave-number range denoted as k_e. These results can provide important guidance to achieve sophisticated nanostructures for functional devices in a single fiber or integrated fabrics.

DOI: 10.1103/PhysRevFluids.9.123902

I. INTRODUCTION

Thin liquid sheets are ubiquitous in nature. Examples include the flow of water or lava under gravity, the mucous membranes in animal bodies, and even the seemingly insignificant act of blinking, which requires movement on the thin film over the cornea. [1–3]. Oron *et al.* [1] conducted a thorough survey on the linear and nonlinear stability analysis of numerous macroscopic liquid

*Contact author: brxu@fudan.edu.cn
†Contact author: fuqingfei@buaa.edu.cn

films prior to the mid-1990s. Craster and Matar [3] provided an extensive review on the stability and rupture of liquid films.

The stability analysis of liquid sheets has been studied by many researchers. Squire [4] conducted the pioneering theoretical study on the stability of planar liquid films, obtaining the dispersion curve through linear stability analysis. Following this, Hagerty *et al.* [5] conducted additional investigations into the stability of planar liquid sheets. Their theoretical analysis demonstrated that the linear stability analysis of planar liquid sheets reveals two modes of perturbation: the sinuous mode, referred to as the antisymmetric mode, and the varicose mode, referred to as the symmetric mode. In order to more realistically capture the behavior of liquid sheets, Lin [6] and Li [7,8], performed linear stability analyses that included the effects of viscosity. Moreover, Li [8] delved deeper into the relationship between temporal and spatial growth rates, noting that for inviscid fluids the dimensionless temporal growth rate is essentially similar to the spatial growth rate. Brown [9] carried out experiments to study the stability of planar liquid sheets. Mitra *et al.* [10] developed a "dual-mode instability" theory by considering the fluctuations of both sinuous and varicose modes. However, Mitra himself acknowledged the limitations of his study, as the linear stability analysis is applicable only to scenarios where perturbations remain small in the initial stages. Thus, the neglect of nonlinear effects is reasonable in this context. However, as the liquid sheet approaches rupture, nonlinear effects become significant, rendering linear stability analysis inappropriate. Asare *et al.* [11] also highlighted this issue in their earlier study. Dyson *et al.* [12] investigated the stability of bilayer liquid sheets under the long-wave approximation and disregarding the surrounding ambient gas. Building upon Dyson's work, Ye [13] supplemented the effect of ambient gas viscosity on liquid sheet stability.

The aforementioned work analyzed the linear stability of a liquid sheet, well predicting the onset instability in the initial stages. High-order perturbations and nonlinear evolution become significant as the liquid sheet approaches rupture. Matsuuchi [14] investigated the harmonic instability of inviscid liquid in a vacuum. By introducing a long-wave assumption and abandoning the limitation of small perturbations, the second-order equation was solved, revealing that higher-order harmonics induce highly unstable liquid sheets. Subsequently, Clark and Dombrowski [15] studied the instability of inviscid liquid sheets in motion in air, finding that the second-order perturbation induced by linear sinuous mode disturbance results in varicose, which explained the rupture of the liquid sheet. Continuing this approach, Jazayeri [16] extended the perturbation analysis to the third order. Yang *et al.* [17,18], conducted an investigation on the weakly nonlinear instability of viscous and inviscid liquid sheets, and obtained second-order perturbative solutions for surface disturbances. This study revealed that the first-order harmonic of the linear sinuous mode for viscous sheets results in the sinuous mode, similarly to inviscid sheets. Subsequently, Wang [19] extended this research by considering dual modes, and compared the stability analysis results of weak nonlinear analysis and numerical simulations for flat liquid sheets. The outcomes demonstrated that weakly nonlinear analysis had a high degree of accuracy in predicting the thinning shape of perturbation evolution most of the time, and qualitatively explained the instability mechanism of sheet rupture.

In recent years, significant research efforts have been devoted to investigate complex multifluid systems for the fabrication of micro/nanostructures in fibers through thermal drawing [20–25]. Thermal drawing is a fiber manufacturing process in which a macroscopic multimaterial structure (a designed preform) is heated and then drawn down to microscopic scale in cross section. The typical compatible materials, polymer/glass pairs [polyethersulfone (PES)/As_2Se_3 and polyurethane (PUS)/Se], together with additional metals and semiconductors, have been fabricated into versatile functional nanodevices through thermal drawing [23]. In general, the high viscosity of the material suppresses the typical Rayleigh-Plateau capillary instability during thermal drawing [26,27]. Consequently, both the cross-sectional structure and geometry are well preserved from the initial preforms to the final fiber with only a scaling down to microscale during the stretching process (for multilayer planar sheets [25] and multilayer cylindrical sheets [20–24]). However, when the thickness of a liquid sheet is further reduced to the nanoscale, instability may still persist, in multilayer planar sheets [28] and multilayer cylindrical sheets [26,29]. As an example, in the

PES/As_2Se_3/PES structure, a remarkable filamentation instability is observed when the thickness of the As_2Se_3 sheet is reduced to 10 nm, leading to the formation of a set of continuous and orderly arranged filaments [28,29]. Esposito *et al.* further proposed the controlled filamentation instability via a textured structure in the preforms [30].

The filamentation instability observed typically occurs at a low Reynolds number, $\mathrm{Re} \ll 1$. Under such conditions, capillary instability due to the different velocities of liquid layers is not related to the filamentation instability observed in this work [4], suggesting that additional contributing factors should be considered. Notably, the instability observed at the scale of hundreds of nanometers is reminiscent of the spinodal dewetting phenomenon. Different types of dewetting phenomena have been summarized and discussed by De Gennes *et al.* [31]. For films thinner than 1 μm, van der Waals forces play a prominent role in causing the spinodal dewetting. To explain the filamentation instability, a linear stability analysis on a simplified three-layer fiber considering both van der Waals forces and stretching effects was performed by Xu [32], which demonstrated excellent agreement with experimental results. Two key assumptions were made in this work. First, the dewetting instability of multilayer cylindrical sheets could be treated as that of multilayer planar sheets in the thermal drawing process by neglecting curvature effects, since the thickness of the sandwich layer proved to be much smaller than the radius. Second, the outer high-viscosity polymer layer was much thicker than the sandwich layer, so the two outer polymer layers could be treated as extending into infinity as the surrounding fluid. Subsequently, Xu [33] further analyzed the dewetting instability of composite multilayer liquid sheets based on linear analysis.

However, the linear stability analysis is limited to predicting the onset instability at initial stages and cannot predict the nonlinear evolution over an extended period. Therefore, to precisely control the filamentation instability or pattern formation in the fiber, it is necessary to study the nonlinear evolution during thermal drawing. Following the method of perturbation total growth by integrating the local perturbation growth rate along the whole stretching region [32,34], a nonlinear instability of the liquid sheet becomes indispensable before combining the stretching effect. Moreover, Xu primarily focuses on the varicose mode, which is reasonable for linear dewetting stability analysis since the contribution of the sinuous mode is negligible. However, under nonlinear conditions, the harmonic of the sinuous mode presents as a varicose mode [15]. It is necessary to consider the coexistence of both modes in the nonlinear instability of three-layer nanoscale composite planar liquid sheets. This analysis holds significant implications for polymer sheet production in multilayer coextrusion processes. It facilitates the prediction of dimensions and the design of nanostructures with specific shapes, among other applications [32,33].

To solve these problems, in this paper, the second-order nonlinear stability analysis of three-layer planar sheets is performed, considering the coexisting of varicose and sinuous modes. This study will serve as an exploratory endeavor. In Sec. II, the mathematical model and nonlinear solution are presented. In Sec. III, the first-order and second-order results are presented. The dominant mode, the effects of various parameters on the surface wave, and the contribution of the first-order and second-order terms to the surface wave development are discussed. In Sec. IV, the theoretical results obtained in this study are applied to fiber thermal drawing, including predicting the nanowire diameter, studying the effects of arbitrary microperturbations, and producing special fibers with nanostructures. Finally, Sec. V provides a summary of the main findings.

II. MATHEMATICAL MODEL

The nanothread manufacturing process is shown in Fig. 1(a) [30], involving sheet encapsulation between upper and lower substrates to form a sandwich-like preform. Subsequently, the preform is thermally stretched to the microscale, and the sheet will transform into a liquid state. Our research focuses on the instability development of these stretched liquid sheets at the microscale. Considering the substantial thickness disparity between the substrate and the intermediate sheets, the outer polymer layers are treated as infinitely thick. Section II A presents the corresponding mathematical model, including the governing equations and boundary conditions.

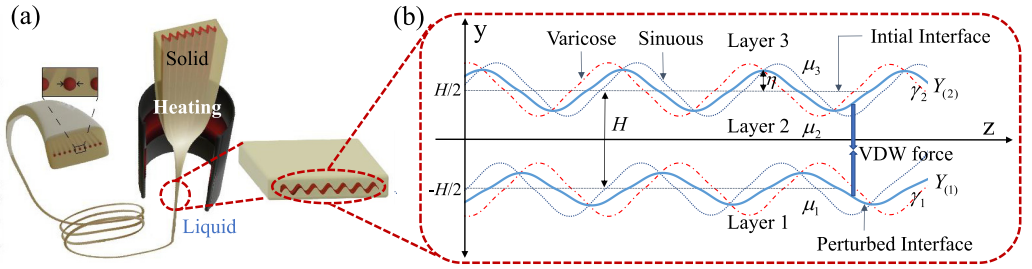

FIG. 1. (a) The manufacturing process of nanowires [30]. (b) A schematic diagram of a three-Layer planar liquid sheet considering varicose and sinuous modes of perturbation and van der Waals force, with significantly larger thickness of the outer fluid layer compared to the middle fluid layer.

A. Governing equations and interfacial conditions

Here we consider two-dimensional planar viscous sheets, with the chosen coordinate system where the z axis is parallel to the flow direction, the y axis is perpendicular to the plane of the sheet, and the origin is located at the midplane, as shown in Fig. 1(b). The viscosities of three layers are μ_1, μ_2, and μ_3 respectively, and the interfacial tension coefficients at the two interfaces are γ_1 and γ_2. Considering the substantial thickness disparity between the substrate and the intermediate sheets, the thickness of the first and third layers is assumed to be infinite, while that of the middle layer is H. Hence, the boundary conditions we are primarily concerned with pertain exclusively to the two interfaces of the middle layer. In subsequent equations, the subscript j denotes the jth layer and the subscript (i) denotes the ith interface. Since the thickness of the liquid sheet is at the nanometer scale, the van der Waals force, as a long-range force, dominates this instability of three-layer nanoscale composite planar liquid sheets. In addition, both varicose and sinuous modes are considered simultaneously.

The governing equations for this planar viscous sheet are

$$\frac{\partial \boldsymbol{u}_j}{\partial t} + (\boldsymbol{u}_j \cdot \nabla)\boldsymbol{u}_j = -\frac{1}{\rho_j}\nabla p_j + \frac{1}{\rho_j}\nabla \boldsymbol{\tau}_j, \tag{1}$$

$$\nabla \boldsymbol{u}_j = 0, \tag{2}$$

where $\boldsymbol{u}_j = (v_j, w_j)$ refers to the velocity vector, $\nabla = (\partial/\partial y, \partial/\partial z)$ refers to the gradient operator, ρ_j represents the density, p_j represents the pressure, and $\boldsymbol{\tau}_j = \boldsymbol{u}_j[\nabla \boldsymbol{u}_j + (\nabla \boldsymbol{u}_j)^T]$ represents the viscous shear stress tensor.

At the ith interface, the unit normal and tangent vectors are denoted as $\boldsymbol{n}_{(i)}$ and $\boldsymbol{t}_{(i)}$, respectively, with the positive direction aligned consistently with that of the coordinate axis. The four boundary conditions at the interfaces can be categorized as two kinematic boundary conditions and two dynamic boundary conditions. The first kinematic boundary condition stipulates that the velocity component perpendicular to the interface is continuous over the entire interface, which can be expressed as

$$\begin{aligned}\boldsymbol{n}_{(i)} \cdot \boldsymbol{u}_j = \boldsymbol{n}_{(i)} \cdot \boldsymbol{u}_{j+1} &= \frac{\mathrm{D}Y_{(i)}}{\mathrm{D}t} = \frac{\partial \boldsymbol{Y}_{(i)}}{\partial t} + (\boldsymbol{u}_j \cdot \nabla)\boldsymbol{Y}_{(i)} \\ &= \frac{\partial \boldsymbol{Y}_{(i)}}{\partial t} + (\boldsymbol{u}_{j+1} \cdot \nabla)\boldsymbol{Y}_{(i)} \quad \text{at } y = \boldsymbol{Y}_{(i)}(z,t).\end{aligned} \tag{3}$$

Second, as a result of the no-slip boundary condition, the continuity of the tangential component of velocity at the interface is ensured

$$\boldsymbol{u}_j \cdot \boldsymbol{t}_{(i)} = \boldsymbol{u}_{j+1} \cdot \boldsymbol{t}_{(i)} \quad \text{at } y = \boldsymbol{Y}_{(i)}(z,t). \tag{4}$$

Additionally, continuity of tangential stress must be sustained at the interface of the fluid sheet:

$$\boldsymbol{n}_{(i)} \cdot \boldsymbol{\tau}_j \cdot \boldsymbol{t}_{(i)} = \boldsymbol{n}_{(i)} \cdot \boldsymbol{\tau}_{j+1} \cdot \boldsymbol{t}_{(i)} \quad \text{at } y = \boldsymbol{Y}_{(i)}(x, z, t). \tag{5}$$

Ultimately, the equilibrium of normal surface stresses across the interface is maintained, accounting for the pressure jump due to surface tension and the impact of van der Waals forces between the upper and lower surfaces of the second liquid layer:

$$p_j - \boldsymbol{n}_{(i)}(\boldsymbol{\tau}_j - \boldsymbol{\tau}_{j+1})\boldsymbol{n}_{(i)} - p_{j+1} = \gamma_{(i)}\boldsymbol{\kappa}_{(i)} - \frac{dV(H)}{dH} \quad \text{at } y = \boldsymbol{Y}_{(i)}(z, t), \tag{6}$$

where the average interface curvature, $\boldsymbol{\kappa}_{(i)} = \nabla \boldsymbol{n}_{(i)}$, can be determined directly from the unit normal vector. The van der Waals force, which can be defined as the potential energy per unit area $V(H)$ and expressed as a function of thickness H, is typically represented by the Hamaker constant A,

$$V(H) = -\frac{A}{12\pi H^2}. \tag{7}$$

In addition, expressions for the unit normal and unit tangential vectors are also provided here. The unit normal vector $\boldsymbol{n}_{(i)}$ can be directly obtained:

$$\boldsymbol{n}_{(i)} = \left(\frac{1}{\sqrt{1 + (\partial Y_{(i)}/\partial z)^2}}, -\frac{\partial Y_{(i)}}{\partial z} \frac{1}{\sqrt{1 + (\partial Y_{(i)}/\partial z)^2}} \right). \tag{8}$$

Then the unit tangential vector is

$$\boldsymbol{t}_{(i)} = \left(\frac{\partial Y_{(i)}}{\partial z} \frac{1}{\sqrt{1 + (\partial Y_{(i)}/\partial z)^2}}, \frac{1}{\sqrt{1 + (\partial Y_{(i)}/\partial z)^2}} \right). \tag{9}$$

B. Initial flow in steady state

Stokes flow is considered here, for simplicity, the initial flow velocity attains zero in the steady state case. Consequently, the velocity of the liquid sheet and outer fluid reaches $\bar{\boldsymbol{u}}_j = 0$ in a steady state. In such a state, the stress tensor is $\bar{\boldsymbol{\tau}}_j = 0$. Moreover, the planar multilayer fluid sheet interface remains parallel to the z direction at $y = \boldsymbol{Y}_{(i)}(z, t)$ in a steady state. The corresponding unit normal and unit tangent vectors are $\bar{\boldsymbol{n}}_j = (1, 0)$ and $\bar{\boldsymbol{t}}_j = (0, 1)$, respectively.

C. Nonlinear perturbation theory

Perturbation method is applied to tackle the system of equations specified in Sec. II A. The underlying assumption is that all perturbations can be expressed as a power series of initial perturbation amplitudes denoted as η_0. Taking weak nonlinearity into account, this paper limits the expansion of perturbations to second order:

$$\begin{bmatrix} \boldsymbol{u}_j \\ p_j \\ \boldsymbol{\tau}_j \\ Y_j \\ \boldsymbol{n}_j \\ \boldsymbol{t}_j \end{bmatrix} = \begin{bmatrix} \bar{\boldsymbol{u}}_j \\ \bar{p}_j \\ \bar{\boldsymbol{\tau}}_j \\ \bar{Y}_j \\ \bar{\boldsymbol{n}}_j \\ \bar{\boldsymbol{t}}_j \end{bmatrix} + \begin{bmatrix} {}^1\tilde{\boldsymbol{u}}_j \\ {}^1\tilde{p}_j \\ {}^1\tilde{\boldsymbol{\tau}}_j \\ {}^1\tilde{Y}_j \\ {}^1\tilde{\boldsymbol{n}}_j \\ {}^1\tilde{\boldsymbol{t}}_j \end{bmatrix} \cdot \eta_0 + \begin{bmatrix} {}^2\tilde{\boldsymbol{u}}_j \\ {}^2\tilde{p}_j \\ {}^2\tilde{\boldsymbol{\tau}}_j \\ {}^2\tilde{Y}_j \\ {}^2\tilde{\boldsymbol{n}}_j \\ {}^2\tilde{\boldsymbol{t}}_j \end{bmatrix} \cdot \eta_0^2. \tag{10}$$

The superscripts "1" and "2" in the upper left corner represent first-order terms and second-order terms respectively. In fact, ${}^1\tilde{\boldsymbol{\tau}}_j$, ${}^1\tilde{\boldsymbol{n}}_j$, and ${}^1\tilde{\boldsymbol{t}}_j$ can be directly calculated from ${}^1\tilde{\boldsymbol{u}}_j$ and ${}^1\tilde{Y}_j$. In order to facilitate the expression of the first-order and second-order perturbation equations, the above expansion is made.

Substituting (10) into Eqs. (1)–(6) and extracting the coefficients of η_0 and η_0^2. Considering that the flow of the planar liquid sheet here is in the form of Stokes flow, the inertial terms in the control equations are neglected. The obtained first-order equations are

$$0 = -\frac{1}{\rho_j}\nabla \cdot ({}^1\tilde{p}_j) + \frac{\mu_j}{\rho_j}\nabla^2 \cdot ({}^1\tilde{\boldsymbol{u}}_j), \tag{11}$$

$$\nabla \cdot ({}^1\tilde{\boldsymbol{u}}_j) = 0, \tag{12}$$

$${}^1\tilde{\boldsymbol{u}}_i \cdot \bar{\boldsymbol{n}}_{(i)} = {}^1\tilde{\boldsymbol{u}}_{i+1} \cdot \bar{\boldsymbol{n}}_{(i)} = \frac{\partial({}^1\tilde{Y}_{(i)})}{\partial t} \quad \text{at } y = \bar{\boldsymbol{Y}}_{(i)}(x, z, t), \tag{13}$$

$${}^1\tilde{\boldsymbol{u}}_i \cdot \bar{\boldsymbol{t}}_{(i)} = {}^1\tilde{\boldsymbol{u}}_{i+1} \cdot \bar{\boldsymbol{t}}_{(i)} \quad \text{at } y = \bar{\boldsymbol{Y}}_{(i)}(x, z, t), \tag{14}$$

$$\bar{\boldsymbol{n}}_{(i)} \cdot {}^1\tilde{\boldsymbol{\tau}}_i \cdot \bar{\boldsymbol{t}}_{(i)} = \bar{\boldsymbol{n}}_{(i)} \cdot {}^1\tilde{\boldsymbol{\tau}}_{i+1} \cdot \bar{\boldsymbol{t}}_{(i)} \quad \text{at } y = \bar{\boldsymbol{Y}}_{(i)}(x, z, t), \tag{15}$$

$${}^1\tilde{p}_i - \bar{\boldsymbol{n}}_{(i)} \cdot ({}^1\tilde{\boldsymbol{\tau}}_i - {}^1\tilde{\boldsymbol{\tau}}_{i+1}) \cdot \bar{\boldsymbol{n}}_{(i)} - {}^1\tilde{p}_{i+1} = -\gamma_{(i)}\frac{\partial^2 \cdot ({}^1\tilde{Y}_{(i)})}{\partial z^2} + \frac{A \cdot {}^1\tilde{H}}{2\pi H^4} \quad \text{at } y = \bar{\boldsymbol{Y}}_{(i)}(x, z, t), \tag{16}$$

where ${}^1\tilde{H} = {}^1\tilde{Y}_{(2)} - {}^1\tilde{Y}_{(1)}$. The second-order equations are

$$0 = -\frac{1}{\rho_j}\nabla \cdot ({}^2\tilde{p}_j) + \frac{\mu_j}{\rho_j}\nabla^2 \cdot ({}^2\tilde{\boldsymbol{u}}_j), \tag{17}$$

$$\nabla \cdot ({}^2\tilde{\boldsymbol{u}}_j) = 0, \tag{18}$$

$$\begin{aligned} {}^2\tilde{\boldsymbol{u}}_i \cdot \bar{\boldsymbol{n}}_{(i)} + {}^1\tilde{\boldsymbol{u}}_i \cdot {}^1\tilde{\boldsymbol{n}}_{(i)} &= {}^2\tilde{\boldsymbol{u}}_{i+1} \cdot \bar{\boldsymbol{n}}_{(i)} + {}^1\tilde{\boldsymbol{u}}_{i+1} \cdot {}^1\tilde{\boldsymbol{n}}_{(i)} = \frac{\partial({}^2\tilde{Y}_{(i)})}{\partial t} + ({}^1\tilde{\boldsymbol{u}}_i \cdot \nabla)\tilde{\boldsymbol{Y}}_{(i)} \\ &= \frac{\partial({}^2\tilde{Y}_{(i)})}{\partial t} + ({}^1\tilde{\boldsymbol{u}}_{i+1} \cdot \nabla)\tilde{\boldsymbol{Y}}_{(i)}, \end{aligned} \tag{19}$$

$${}^2\tilde{\boldsymbol{u}}_i \cdot \bar{\boldsymbol{t}}_{(i)} + {}^1\tilde{\boldsymbol{u}}_i \cdot {}^1\tilde{\boldsymbol{t}}_{(i)} = {}^2\tilde{\boldsymbol{u}}_{i+1} \cdot \bar{\boldsymbol{t}}_{(i)} + {}^1\tilde{\boldsymbol{u}}_{i+1} \cdot {}^1\tilde{\boldsymbol{t}}_{(i)}, \tag{20}$$

$$\begin{aligned} &\bar{\boldsymbol{n}}_{(i)} \cdot {}^2\tilde{\boldsymbol{\tau}}_i \cdot \bar{\boldsymbol{t}}_{(i)} + {}^1\tilde{\boldsymbol{n}}_{(i)} \cdot {}^1\tilde{\boldsymbol{\tau}}_i \cdot \bar{\boldsymbol{t}}_{(i)} + \bar{\boldsymbol{n}}_{(i)} \cdot {}^1\tilde{\boldsymbol{\tau}}_i \cdot {}^1\tilde{\boldsymbol{t}}_{(i)} \\ &= \bar{\boldsymbol{n}}_{(i)} \cdot {}^2\tilde{\boldsymbol{\tau}}_{i+1} \cdot \bar{\boldsymbol{t}}_{(i)} + {}^1\tilde{\boldsymbol{n}}_{(i)} \cdot {}^1\tilde{\boldsymbol{\tau}}_{i+1} \cdot \bar{\boldsymbol{t}}_{(i)} + \bar{\boldsymbol{n}}_{(i)} \cdot {}^1\tilde{\boldsymbol{\tau}}_{i+1} \cdot {}^1\tilde{\boldsymbol{t}}_{(i)}, \end{aligned} \tag{21}$$

$$\begin{aligned} &{}^2\tilde{p}_i - {}^2\tilde{p}_{i+1} - \bar{\boldsymbol{n}}_{(i)} \cdot ({}^2\tilde{\boldsymbol{\tau}}_i - {}^2\tilde{\boldsymbol{\tau}}_{i+1}) \cdot \bar{\boldsymbol{n}}_{(i)} - {}^1\tilde{\boldsymbol{n}}_{(i)} \cdot ({}^1\tilde{\boldsymbol{\tau}}_i - {}^1\tilde{\boldsymbol{\tau}}_{i+1}) \cdot \bar{\boldsymbol{n}}_{(i)} - \bar{\boldsymbol{n}}_{(i)} \cdot ({}^1\tilde{\boldsymbol{\tau}}_i - {}^1\tilde{\boldsymbol{\tau}}_{i+1}) \cdot {}^1\tilde{\boldsymbol{n}}_{(i)} \\ &= -\gamma_{(i)}\frac{\partial^2 \cdot ({}^2\tilde{Y}_{(i)})}{\partial z^2} + \frac{A \cdot {}^2\tilde{H}}{2\pi H^4} - \frac{A \cdot {}^1\tilde{H}^2}{\pi H^5} \quad \text{at } y = \bar{\boldsymbol{Y}}_{(i)}(x, z, t). \end{aligned} \tag{22}$$

Additionally, the form of the initial interface displacement is

$${}^1\bar{\eta}_j|_{t=0} = \bar{\eta}_j e^{ikz} + \text{c.c.}, \tag{23}$$

$${}^2\bar{\eta}_j|_{t=0} = 0, \tag{24}$$

where ${}^1\bar{\eta}_j|_{t=0}$ and ${}^2\bar{\eta}_j|_{t=0}$ are the first-order and second-order initial displacements respectively.

All nonlinear terms in the second-order equations are composed of the first-order variables. Therefore, these nonlinear terms can be substituted to obtain the solution after solving the first-order equations.

D. The solution of the first-order equations

Before solving, it should be pointed out that in the actual process the outer fluids 1 and 3 have the same physical composition ($\mu_1 = \mu_3$, $\rho_1 = \rho_3$, $\gamma_1 = \gamma_2$) [30].

The first-order equations are linear and can be solved using standard linear stability analysis methods. The solution to the first-order equations conforms to the following form:

$$\begin{bmatrix} {}^1\tilde{\boldsymbol{u}}_j \\ {}^1\tilde{p}_j \\ {}^1\tilde{\boldsymbol{Y}}_j \end{bmatrix} = \begin{bmatrix} {}^1\tilde{\boldsymbol{U}}_j \\ {}^1\tilde{P}_j \\ {}^1\tilde{\boldsymbol{\eta}}_j \end{bmatrix} \exp(\omega_1 t + ikz) + \text{c.c.}, \tag{25}$$

where k is the wave number of perturbations, and the real part of ω_1 corresponds to the growth rate of the perturbations.

In order to solve the Eqs. (11)–(16), this study introduces a stream function,

$$\tilde{v}_j = \frac{\partial \tilde{\phi}_j}{\partial z}, \quad \tilde{w}_j = -\frac{\partial \tilde{\phi}_j}{\partial z}. \tag{26}$$

Upon substitution of Eq. (25) into Eq. (11) and subsequent elimination of the pressure term, the following is obtained:

$$\nabla^2 \nabla^2 \tilde{\phi}_j = 0. \tag{27}$$

The perturbations of the stream function can be expressed as $\tilde{\phi}_j = \tilde{\Phi}_j \exp(\omega_1 t + ikz)$. Substituting this expression into Eq. (27) yields

$$\left(\frac{d^2}{dy^2} - k^2\right)^2 \tilde{\Phi}_j = 0. \tag{28}$$

The solution to equation (28) can be expressed in the following general form:

$$\tilde{\Phi}_j = c_{1,j}^{(1)} e^{ky} + c_{2,j}^{(1)} e^{-ky} + c_{3,j}^{(1)} y e^{ky} + c_{4,j}^{(1)} y e^{-ky}. \tag{29}$$

The superscript "(1)" indicates that this is the integration constant of the first-order quantity. Then, substituting Eq. (29) into (26) yields the expression for velocity:

$$\begin{aligned} {}^1\tilde{\boldsymbol{u}}_j &= \begin{bmatrix} {}^1\tilde{\boldsymbol{v}}_j \\ {}^1\tilde{\boldsymbol{w}}_j \end{bmatrix} = \begin{bmatrix} {}^1\tilde{\boldsymbol{V}}_j \\ {}^1\tilde{\boldsymbol{W}}_j \end{bmatrix} e^{w_1 t + ikz} \\ &= \left[ik\left(c_{1,j}^{(1)} e^{ky} + c_{2,j}^{(1)} e^{-ky} + c_{3,j}^{(1)} y e^{ky} + c_{4,j}^{(1)} y e^{-ky}\right)\right. \\ &\quad \left. - \left[kc_{1,j}^{(1)} + (ky+1)c_{3,j}^{(1)}\right] e^{ky} + \left[kc_{2,j}^{(1)} + (ky-1)c_{4,j}^{(1)}\right] e^{-ky}\right] e^{w_1 t + ikz}. \end{aligned} \tag{30}$$

The expression for pressure can be obtained through the momentum equation in the z direction,

$${}^1\tilde{p}_j = 2\mu_j ik\left(+ c_{3,j}^{(1)} y e^{ky} + c_{4,j}^{(1)} y e^{-ky}\right) e^{\omega_1 + ikz}. \tag{31}$$

Subsequently, by substituting the expressions for velocity and pressure given by Eqs. (30) and (31) into the boundary conditions (13)–(16), the following system of equations can be obtained:

$$\begin{aligned} &ik\left(c_{1,j}^{(1)} e^{kY_j} + c_{2,j}^{(1)} e^{-kY_j} + c_{3,j}^{(1)} Y_j e^{kY_j} + c_{4,j}^{(1)} Y_j e^{-kY_j}\right) \\ &\quad = ik\left(c_{1,j+1}^{(1)} e^{kY_j} + c_{2,j+1}^{(1)} e^{-kY_j} + c_{3,j+1}^{(1)} Y_j e^{kY_j} + c_{4,j+1}^{(1)} Y_j e^{-kY_j}\right) = \tilde{\eta}_{1,j}\omega_1, \end{aligned} \tag{32a}$$

$$\begin{aligned} &\left(kc_{1,j}^{(1)} + c_{3,j}^{(1)} + kY_j c_{3,j}^{(1)}\right) e^{kY_j} + \left(- kc_{2,j}^{(1)} + c_{4,j}^{(1)} - kY_j c_{3,j}^{(1)}\right) e^{-kY_j} \\ &\quad = \left(kc_{1,j+1}^{(1)} + c_{3,j+1}^{(1)} + kY_j c_{3,j+1}^{(1)}\right) e^{kY_j} + \left(- kc_{2,j+1}^{(1)} + c_{4,j+1}^{(1)} - kY_j c_{4,j+1}^{(1)}\right) e^{-kY_j}, \end{aligned} \tag{32b}$$

$$\begin{aligned} &\mu_j\left[- c_{1,j}^{(1)} k^2 e^{kY_j} - c_{2,j}^{(1)} k^2 e^{-kY_j} - c_{3,j}^{(1)} k(1+kY_j) e^{kY_j} + c_{4,j}^{(1)} k(1-kY_j) e^{-kY_j}\right] \\ &\quad = \mu_{j+1}\left[- c_{1,j+1}^{(1)} k^2 e^{kY_j} - c_{2,j+1}^{(1)} k^2 e^{-kY_j} - c_{3,j+1}^{(1)} k(1+kY_j) e^{kY_j} + c_{4,j+1}^{(1)} k(1-kY_j) e^{-kY_j}\right], \end{aligned} \tag{32c}$$

$$
\begin{aligned}
&2\mu_j ik\left(c_{3,j}^{(1)}e^{kY_j}+c_{4,j}^{(1)}e^{-kY_j}\right)-2\mu_{j+1}ik\left(c_{3,j+1}^{(1)}e^{kY_j}+c_{4,j+1}^{(1)}e^{-kY_j}\right)\\
&-2\mu_j ik^2\left[c_{1,j}^{(1)}ke^{kY_j}-c_{2,j}^{(1)}ke^{-kY_j}+c_{3,j}^{(1)}(1+kY_j)e^{kY_j}+c_{4,j}^{(1)}(1-kY_j)e^{-kY_j}\right]\\
&+2\mu_{j+1}ik^2\left[c_{1,j+1}^{(1)}ke^{kY_j}-c_{2,j+1}^{(1)}ke^{-kY_j}+c_{3,j+1}^{(1)}(1+kY_j)e^{kY_j}+c_{4,j+1}^{(1)}(1-kY_j)e^{-kY_j}\right]\\
&=\gamma_j\tilde{\eta}_j k^2+\frac{A(\tilde{\eta}_2-\tilde{\eta}_1)}{2\pi H^4},
\end{aligned}
\tag{32d}
$$

at $j=1$, $Y_1=-H/2$ and $j=2$, $Y_1=H/2$. Furthermore, because the speed and pressure are limited at $y\to-\infty$ and $y\to\infty$, one can obtain that $c_{2,1}^{(1)}=c_{4,1}^{(1)}=c_{1,3}^{(1)}=c_{3,3}^{(1)}=0$. The dispersion relation and the integration constants can be obtained by solving Eq. (32).

First, we consider the varicose mode, where perturbations at both interfaces are ${}^{1,v}\tilde{\eta}_1=-{}^{1,v}\tilde{\eta}_2=\varepsilon$. The superscript "$v$" denotes the first-order quantity that corresponds to the varicose mode. The expression for the dispersion relation can be obtained as

$$
\omega_1^v=-\frac{k}{2}\left(\gamma-\frac{A}{k^2\pi H^4}\right)\frac{\mu_2(\cosh(kH)-1)+\mu_1(\sinh(kH)-kH)}{\mu_2^2[\sinh(kH)+kH]+2\mu_1\mu_2\cosh(kH)+\mu_1^2[\sinh(kH)-kH]}. \tag{33}
$$

Then, the result for the integration constant is provided

$$
c_{1,1}^{(1),v}=-c_{2,3}^{(1),v}=-\frac{{}^{1,v}\tilde{\eta}_1\omega_1^v}{2ik}\frac{C_{v1}}{B_v}e^{kH/2}, \tag{34a}
$$

$$
c_{3,1}^{(1),v}=c_{4,3}^{(1),v}=i^{1,v}\tilde{\eta}_1\omega_1^v\frac{C_{v2}}{B_v}e^{kH/2}, \tag{34b}
$$

$$
c_{1,2}^{(1),v}=-c_{2,2}^{(1),v}=-\frac{{}^{1,v}\tilde{\eta}_1\omega_1^v}{2ik}\frac{C_{v3}}{B_v}e^{kH/2}, \tag{34c}
$$

$$
c_{3,2}^{(1),v}=c_{4,2}^{(1),v}=-i^{1,v}\tilde{\eta}_1\omega_1^v\frac{C_{v4}}{B_v}e^{kH/2}, \tag{34d}
$$

$$
c_{2,1}^{(1),v}=c_{4,1}^{(1),v}=c_{1,3}^{(1),v}=c_{3,3}^{(1),v}=0, \tag{34e}
$$

where C_{v1}, C_{v2}, C_{v3}, C_{v4}, and B_v are

$$
\begin{aligned}
C_{v1}&=\mu_1(kH-2)(-1+e^{2kH}-2e^{kH}kH)+\mu_2(kH-2)(-1+e^{kH})^2+2\mu_2k^2H^2e^{kH},\\
C_{v2}&=\mu_1(-1+e^{2kH}-2e^{kH}kH)+\mu_2(-1+e^{kH})^2+2\mu_2kHe^{kH},\\
C_{v3}&=(2-kH)(\mu_1-\mu_2)+(2+kH)(\mu_1+\mu_2)e^{kH},\\
C_{v4}&=(1+e^{kH})\mu_1+(-1+e^{kH})\mu_2,\\
B_v&=\mu_1(-1+e^{2kH}-2e^{kH}kH)+\mu_2(-1+e^{kH})^2,
\end{aligned}
$$

Then, the sinuous mode with perturbations at both interfaces ${}^{1,s}\tilde{\eta}_1={}^{1,s}\tilde{\eta}_2=\varepsilon$ is considered. The superscript "s" denotes the first-order quantity that corresponds to the sinuous mode.

The expression for the dispersion relation can be obtained as

$$
\omega_1^s=-\frac{\gamma_1 k}{4}\frac{kH\mu_1+\mu_2+\mu_2\cosh(kH)+\mu_1\sinh(kH)}{kH(\mu_1-\mu_2)(\mu_1+\mu_2)+2\mu_1\mu_2\cosh(kH)+\left(\mu_1^2+\mu_2^2\right)\sinh(kH)}. \tag{35}
$$

The expression for the dispersion relation can be obtained as

$$c_{1,1}^{(1),s} = c_{2,3}^{(1),s} = \frac{i^{1,s}\tilde{\eta}_1\omega_1^s}{2k}\frac{C_{s1}}{B_s}e^{kH/2}, \tag{36a}$$

$$c_{3,1}^{(1),s} = -c_{4,3}^{(1),s} = i^{1,s}\tilde{\eta}_1\omega_1^s\frac{C_{s2}}{B_s}e^{kH/2}, \tag{36b}$$

$$c_{1,2}^{(1),s} = c_{2,2}^{(1),s} = -\frac{i^{1,s}\tilde{\eta}_1\omega_1^s}{4k}\frac{C_{s3}}{B_s}e^{-kH/2}, \tag{36c}$$

$$c_{3,2}^{(1),s} = -c_{4,2}^{(1),s} = i^{1,s}\tilde{\eta}_1\omega_1^s\frac{C_{s4}}{B_s}, \tag{36d}$$

$$c_{2,1}^{(1),s} = c_{4,1}^{(1),s} = c_{1,3}^{(1),s} = c_{3,3}^{(1),s} = 0, \tag{36e}$$

where C_{s1}, C_{s2}, C_{s3}, C_{s4}, and B_s are

$$\begin{aligned}
C_{s1} &= \mu_1(kH-2)[kH+\sinh(kH)] + \mu_2(kH-2)[1-kH+\cosh(kH)] - 2\mu_2 kH,\\
C_{s2} &= \mu_1[kH+\sinh(kH)] + \mu_2[1-kH+\cosh(kH)],\\
C_{s3} &= (-2+kH)(\mu_1-\mu_2) + e^{kH}(2+kH)(\mu_1+\mu_2),\\
C_{s4} &= \mu_1\sinh(kH/2) + \mu_2\cosh(kH/2),\\
B_s &= \mu_1[kH+\sinh(kH)] + \mu_2[1+\cosh(kH)].
\end{aligned}$$

After obtaining the solutions for both modes, the first-order results are further summarized in this study. In contrast to previous investigations, which only considered the wave dynamics of a single mode, the present work examines the situation in which both modes coexist in the linear part. As such, the solution for the linear part is derived as follows:

$$\begin{bmatrix} {}^1\tilde{\boldsymbol{u}}_j \\ {}^1\tilde{p}_j \\ {}^1\tilde{\boldsymbol{Y}}_j \end{bmatrix} = \begin{bmatrix} {}^{1,s}\tilde{\boldsymbol{U}}_j(y) \\ {}^{1,s}\tilde{P}_j(y) \\ {}^{1,s}\tilde{\boldsymbol{\eta}}_{(i)} \end{bmatrix} \exp\left(\omega_1^s t + ik_1^s z\right) + \begin{bmatrix} {}^{1,v}\tilde{\boldsymbol{U}}_j(y) \\ {}^{1,v}\tilde{P}_j(y) \\ {}^{1,v}\tilde{\boldsymbol{\eta}}_{(i)} \end{bmatrix} \exp\left(\omega_1^v t + ik_1^v z\right). \tag{37}$$

where the superscript s denotes the sinuous mode and the superscript v refers to the varicose mode.

Considering the temporal instability, it can be inferred that [19]

$$k_1^s = k_1^v = k. \tag{38}$$

In order to quantify the initial proportion of the tensor mode in first-order perturbations, the r_v are defined here

$$r_v = \frac{|{}^{1,v}\tilde{\eta_{(i)}}|}{|{}^{1,v}\tilde{\eta_{(i)}}| + |{}^{1,s}\tilde{\eta_{(i)}}|}. \tag{39}$$

The range of values for r_v is $0 < r_v < 1$. When $r_v = 1$, only varicose modes exist in linear perturbations. When $r_v = 0$, only sinuous modes exist in linear perturbations.

E. The solution of the second-order equations

The inhomogeneous terms in the second-order equations, specified by Eqs. (17)–(22), are entirely constituted of first-order terms. Meanwhile, the results of the first-order terms have been already computed in Sec. II D. Therefore, the second-order equations take the form of nonhomogeneous linear equations when applied to unknown second-order perturbations. Setting $(\tilde{\boldsymbol{X}}_j) = (\tilde{\boldsymbol{U}}_j, \tilde{\boldsymbol{P}}_j, \tilde{\boldsymbol{\eta}}_j)$, the general solution of this system of homogeneous linear equations should satisfy the form

$$({}^{21}\tilde{\boldsymbol{x}}_j) = ({}^{21}\tilde{\boldsymbol{X}}_j)\exp(\omega_2 t + 2ikz) + \text{c.c.}, \tag{40}$$

where superscript 21 indicates the general solution. The particular solution introduced by the inhomogeneous term should conform to the form

$$({}^{22}\tilde{\boldsymbol{x}}_j) = [({}^{22}\tilde{\boldsymbol{X}}_j)\exp(\omega_1 t + ikz) + \text{c.c.}] \times [({}^{22}\tilde{\boldsymbol{X}}_j)\exp(\omega_1 t + ikz) + \text{c.c.}], \tag{41}$$

where superscript 22 indicates the particular solution. Considering that the sinuous mode and the varicose mode exist simultaneously in the linear part, this means that the general solution of the second-order homogeneous linear equation is

$$({}^{21}\tilde{\boldsymbol{x}}_j) = \left[({}^{21,ss}\tilde{\boldsymbol{X}}_j)\exp\left(\omega_2^s t + 2ikz\right) + \text{c.c.}\right] + \left[({}^{21,vv}\tilde{\boldsymbol{X}}_j)\exp\left(\omega_2^v t + 2ikz\right) + \text{c.c.}\right]. \tag{42}$$

For the particular solution part, replace $[\exp(\omega_1 t + ikz) + \text{c.c.}]$ with $[\exp(\omega_1^s t + ikz) + \text{c.c.}] \times [\exp(\omega_1^v t + ikz) + \text{c.c.}]$. Then, the solution to the second-order equations can be expressed as

$$\begin{aligned}({}^{2}\tilde{\boldsymbol{x}}_j) = {} & ({}^{21,ss}\tilde{\boldsymbol{X}}_j)\exp\left(\omega_2^s t + 2ikz\right) + ({}^{21,vv}\tilde{\boldsymbol{X}}_j)\exp\left(\omega_2^v t + 2ikz\right) + \text{c.c.} \\ & + \left[({}^{22,s}\tilde{\boldsymbol{X}}_j)\exp\left(\omega_1^s t + ikz\right) + ({}^{22,v}\tilde{\boldsymbol{X}}_j)\exp\left(\omega_1^v t + ikz\right) + \text{c.c.}\right] \\ & \times \left[({}^{22,s}\tilde{\boldsymbol{X}}_j)\exp\left(\omega_1^s t + ikz\right) + ({}^{22,v}\tilde{\boldsymbol{X}}_j)\exp\left(\omega_1^v t + ikz\right) + \text{c.c.}\right].\end{aligned} \tag{43}$$

After simplification, we obtain

$$\begin{aligned}&({}^{2}\tilde{\boldsymbol{u}}_j, {}^{2}\tilde{p}_j, {}^{2}\tilde{Y}_{(i)}) \\ &= ({}^{21,ss}\tilde{\boldsymbol{U}}_j, {}^{21,ss}\tilde{P}_j, {}^{21,ss}\tilde{\eta}_{(i)})\exp\left(\omega_2^s t + 2ikz\right) + ({}^{21,vv}\tilde{\boldsymbol{U}}_j, {}^{21,vv}\tilde{P}_j, {}^{21,vv}\tilde{\eta}_{(i)})\exp\left(\omega_2^v t + 2ikz\right) \\ &\quad + ({}^{22,ss}\tilde{\boldsymbol{U}}_j, {}^{22,ss}\tilde{P}_j, {}^{22,ss}\tilde{\eta}_{(i)})\exp\left(2\omega_1^s t + 2ikz\right) + ({}^{22,vv}\tilde{\boldsymbol{U}}_j, {}^{22,vv}\tilde{P}_j, {}^{22,vv}\tilde{\eta}_{(i)})\exp\left(2\omega_1^v t + 2ikz\right) \\ &\quad + ({}^{22,sv}\tilde{\boldsymbol{U}}_j, {}^{22,sv}\tilde{P}_j, {}^{22,sv}\tilde{\eta}_{(i)})\exp\left(\omega_1^s t + \omega_1^v t + 2ikz\right) + ({}^{23,s\bar{s}}\tilde{\boldsymbol{U}}_j, {}^{23,s\bar{s}}\tilde{P}_j, {}^{23,s\bar{s}}\tilde{\eta}_{(i)})\exp\left(2\omega_{1r}^s t\right) \\ &\quad + ({}^{23,v\bar{v}}\tilde{\boldsymbol{U}}_j, {}^{23,v\bar{v}}\tilde{P}_j, {}^{23,v\bar{v}}\tilde{\eta}_{(i)})\exp\left(2\omega_{1r}^v t\right) + ({}^{23,s\bar{v}}\tilde{\boldsymbol{U}}_j, {}^{23,s\bar{v}}\tilde{P}_j, {}^{23,s\bar{v}}\tilde{\eta}_{(i)})\exp\left(\omega_1^s t + \bar{\omega}_1^v t\right) + \text{c.c.}\end{aligned} \tag{44}$$

The perturbations with superscript 21 represent the second-order intrinsic perturbations, which have second-order growth rates ω_2^s and ω_2^v. The perturbations with superscript 22 are the perturbations that are transmitted from the first order to the second order. The perturbations with superscript 23 are the parts that only change with time. The mention of the second-order term setting pertains to the approach introduced by Wang [19].

First, solve for the term with superscript 22. Taking $\exp(2\omega_1^v t + 2ikz)$ as an example. Substitute (44) into Eqs. (17) to (22) and collect the coefficients of terms containing $\exp(2\omega_1^v t + 2ikz)$. Then, the momentum equation will become

$$-\frac{1}{\rho_j}\nabla\left[{}^{22,vv}\tilde{P}_j \times \exp\left(2\omega_1^v t + 2ikz\right)\right] + \frac{\mu_j}{\rho_j}\nabla^2\left[{}^{22,vv}\tilde{\boldsymbol{U}}_j \times \exp\left(2\omega_1^v t + 2ikz\right)\right], \tag{45}$$

where $\tilde{\boldsymbol{U}}_j = (\tilde{V}_j, \tilde{W}_j)$.

We introduce the flow function:

$${}^{22,vv}\tilde{v}_j = \frac{\partial^{22,vv}\tilde{\phi}_j}{\partial z}, \quad \tilde{w}_j = -\frac{\partial^{22,vv}\tilde{\phi}_j}{\partial z}, \tag{46}$$

where ${}^{22,vv}\tilde{\phi}_j = {}^{22,vv}\tilde{\Phi}_j \exp(2\omega_1^v t + ikz)$. Substituting the flow function into Eq. (45) and eliminating the pressure term yields

$$\nabla^2\nabla^2\left[{}^{22,vv}\tilde{\Phi}_j \exp\left(2\omega_1^v t + ikz\right)\right] = 0. \tag{47}$$

Solving Eq. (47) yields:

$$
\begin{aligned}
{}^{22,vv}\tilde{\boldsymbol{u}}_{1,j} &= \begin{bmatrix} {}^{22,vv}\tilde{\boldsymbol{v}}_{1,j} \\ {}^{22,vv}\tilde{\boldsymbol{w}}_{1,j} \end{bmatrix} = \begin{bmatrix} {}^{22,vv}\tilde{\boldsymbol{V}}_{1,j} \\ {}^{22,vv}\tilde{\boldsymbol{W}}_{1,j} \end{bmatrix} e^{2w_1^v t+ikz} \\
&= \left[2ik\left(c_{1,j}^{(22,vv)}e^{2ky} + c_{2,j}^{(22,vv)}e^{-2ky} + c_{3,j}^{(22,vv)}ye^{2ky} + c_{4,j}^{(22,vv)}ye^{-2ky}\right)\right. \\
&\quad \left. - \left[2kc_{1,j}^{(22,vv)} + (2ky+1)c_{3,j}^{(22,vv)}\right]e^{2ky} + \left[2kc_{2,j}^{(22,vv)} + (2ky-1)c_{4,j}^{(22,vv)}\right]e^{-2ky}\right]e^{2w_1^v t+ikz}.
\end{aligned}
\tag{48}
$$

Substituting (48) into (45) facilitates the computation of the pressure term:

$$
{}^{22,vv}\tilde{p}_j = 4\mu_j ik\left(+c_{3,j}^{(1)}ye^{2ky} + c_{4,j}^{(1)}ye^{-2ky}\right)e^{2\omega_1^v+ikz}. \tag{49}
$$

By substituting (44) into Eqs. (19)–(22) and extracting terms containing only $\exp(2\omega_1^v t + 2ikz)$, the following equations are obtained:

$$
{}^{22,vv}\tilde{V}_j - 2\times {}^{1}\tilde{W}_j \times {}^{1}\tilde{\eta}_j(ik) = {}^{22,vv}\tilde{V}_{j+1} - 2\times {}^{1}\tilde{W}_{j+1} \times {}^{1}\tilde{\eta}_j(ik) = 2\omega_1 \times {}^{22,vv}\tilde{\eta}_j, \tag{50a}
$$

$$
{}^{22,vv}\tilde{W}_j + {}^{1}\tilde{V}_j \times {}^{1}\tilde{\eta}_j(ik) = {}^{22,vv}\tilde{W}_{j+1} + {}^{1}\tilde{V}_{j+1} \times {}^{1}\tilde{\eta}_j(ik), \tag{50b}
$$

$$
\begin{aligned}
&\mu_j\left(2ik \times {}^{22,vv}\tilde{V}_j + \frac{\partial^{22,vv}\tilde{W}_j}{\partial y}\right) + 2ik\mu_j \times {}^{1}\tilde{\eta}_j \times \frac{\partial^{1}\tilde{V}_j}{\partial y} + 2k^2\mu_j \times {}^{1}\tilde{\eta}_j \times {}^{1}\tilde{W}_j \\
&= \mu_{j+1}\left(2ik \times {}^{22,vv}\tilde{V}_{j+1} + \frac{\partial^{22,vv}\tilde{W}_{j+1}}{\partial y}\right) + 2ik\mu_{j+1} \times {}^{1}\tilde{\eta}_j \times \frac{\partial^{1}\tilde{V}_{j+1}}{\partial y} + 2k^2\mu_{j+1} \times {}^{1}\tilde{\eta}_j \times {}^{1}\tilde{W}_{j+1},
\end{aligned}
\tag{50c}
$$

$$
\begin{aligned}
&{}^{22,vv}\tilde{P}_{j+1} - {}^{22,vv}\tilde{P}_j + \left(2\mu_j\frac{\partial^{22,vv}\tilde{V}_j}{\partial y} - 2\mu_{j+1}\frac{\partial^{22,vv}\tilde{V}_{j+1}}{\partial y}\right) \\
&-2ik \times {}^{1}\tilde{\eta}_j\left[\mu_j\left(ik \times {}^{1}\tilde{V}_j + \frac{\partial^{1}\tilde{W}_j}{\partial y}\right) - \mu_{j+1}\left(ik \times {}^{1}\tilde{V}_{j+1} + \frac{\partial^{1}\tilde{W}_{j+1}}{\partial y}\right)\right] \\
&= -4k^2 \times \gamma_j \times {}^{22,vv}\tilde{\eta}_j + \frac{A\tilde{H}_1^2}{\pi H^5} - \frac{A\tilde{H}_2}{2\pi H^4},
\end{aligned}
\tag{50d}
$$

at $j = 1$, $Y_1 = -H/2$ and $j = 2$, $Y_1 = H/2$. The velocity and pressure terms are already obtained in Eqs. (28), (29), (48), and (49). Substituting them into equation (50) and solving yields the solution. Its expression is

$$
{}^{22,vv}\tilde{\eta}_1 = -\frac{e^{-3kH} \times {}^{1,v}\tilde{\eta}_1^2(4\pi e^{kH}k^2H^6D_{v3} - 4Ae^{3kH}D_{v1}D_{v2})}{HD_{v1} \times [-D_{v4} + D_{v5} + D_{v6}\cosh(2kH) + D_{v7}\sinh(2kH)]}, \tag{51}
$$

$$
{}^{22,vv}\tilde{\eta}_2 = -{}^{22,vv}\tilde{\eta}_1. \tag{52}
$$

where D_{v1}, D_{v2}, D_{v3}, D_{v4}, D_{v5}, D_{v6}, and D_{v7} are shown as

$$
\begin{aligned}
D_{v1} &= [kH\mu_1 + \mu_2 - \mu_2\cosh(kH) - \mu_1\sinh(kH)], \\
D_{v2} &= [2kH\mu_1 + \mu_2 - \mu_2\cosh(2kH) - \mu_1\sinh(2kH)], \\
D_{v3} &= \mu_2\omega_1^v[-(\mu_1-\mu_2)^2 + e^{4kH}(\mu_1+\mu_2)^2 - 2e^{2kH}(\mu_1-\mu_2)(2\mu_1+\mu_2)], \\
D_{v4} &= (A - 4\pi\gamma k^2H^4)(2kH\mu_1 + \mu_2), \\
D_{v5} &= 16\pi k^2H^5(\mu_1-\mu_2)(\mu_1+\mu_2)\omega_1^v, \\
D_{v6} &= \mu_2\left[A - 4\pi kH^4\left(\gamma k + 4\mu_1\omega_1^v\right)\right], \\
D_{v7} &= A\mu_1 - 4\pi kH^4\left[\gamma k\mu_1 + 2\left(\mu_1^2+\mu_2^2\right)\omega_1^v\right].
\end{aligned}
$$

Equation (52) indicates that the term $\exp(2\omega_1^v t + 2ikz)$ corresponds to the varicose mode.

Following the above procedure, it is possible to separately solve the systems of equations containing only $\exp(2\omega_1^s + 2ikz)$ or $\exp(\omega_1^s + \omega_1^v + 2ikz)$, obtaining solutions for ${}^{22,ss}\tilde{\eta}_{(i)}$ and ${}^{22,sv}\tilde{\eta}_{(i)}$. The result can be obtained:

$$ {}^{22,ss}\tilde{\eta}_1 = -{}^{22,ss}\tilde{\eta}_2, \quad {}^{22,sv}\tilde{\eta}_1 = {}^{22,sv}\tilde{\eta}_2. \tag{53} $$

To save space, the specific results will be directly presented in dimensionless form in Sec. II F.

The term with superscript 23 can be solved utilizing the same procedure. To save space, the result is provided directly:

$$ {}^{23,s\bar{s}}\tilde{\eta}_{(i)} = 0, \quad {}^{23,v\bar{v}}\tilde{\eta}_{(i)} = 0, \quad {}^{23,s\bar{v}}\tilde{\eta}_{(i)} = 0, \tag{54} $$

which means that these terms has no effect on the development of the disturbance.

Finally, solve for the term with superscript 21, which contains only $\exp(\omega_2^s t + 2ikz)$ and $\exp(\omega_2^s t + 2ikz)$. The ${}^{21,ss}\tilde{\eta}_{(i)}$ and ${}^{21,vv}\tilde{\eta}_{(i)}$, as well as ω_2^s and ω_2^v, can be obtained by solving their system of equations. Here, it's necessary to utilize the initial condition (24):

$$ {}^{21,ss}\tilde{\eta}_{(i)} + {}^{21,vv}\tilde{\eta}_{(i)} + {}^{22,ss}\tilde{\eta}_{(i)} + {}^{22,vv}\tilde{\eta}_{(i)} + {}^{22,sv}\tilde{\eta}_{(i)} + {}^{23,s\bar{s}}\tilde{\eta}_{(i)} + {}^{23,v\bar{v}}\tilde{\eta}_{(i)} + {}^{23,s\bar{v}}\tilde{\eta}_{(i)} = 0. \tag{55} $$

In regard to the ${}^{21,ss}\tilde{\eta}_{(i)}$ and ${}^{21,vv}\tilde{\eta}_{(i)}$, as they are the second-order inherent sinuous mode disturbance and varicose mode disturbance, respectively, we can obtain

$$ {}^{21,ss}\tilde{\eta}_1 = {}^{21,ss}\tilde{\eta}_2, \quad {}^{21,vv}\tilde{\eta}_1 = -{}^{21,vv}\tilde{\eta}_2. \tag{56} $$

Upon substituting (52)–(54) and (56) into Eq. (55), the following results emerge:

$$ {}^{21,ss}\tilde{\eta}_{(i)} = -{}^{22,sv}\tilde{\eta}_{(i)}, \quad {}^{21,vv}\tilde{\eta}_{(i)} = -{}^{22,ss}\tilde{\eta}_{(i)} - {}^{22,vv}\tilde{\eta}_{(i)}. \tag{57} $$

With this, all second-order perturbation amplitudes have been solved. The theoretical outcomes will be presented in dimensionless form in Sec. II F.

Furthermore, with the Eq. (56), two second-order dispersion relations can be derived:

$$ \omega_2^s = -\frac{\gamma_1 k}{2} \frac{\mu_1[\sinh(2kH) + 2kH] + \mu_2[\cosh(2kH) + 1]}{2kH(\mu_1 - \mu_2)(\mu_1 + \mu_2) + 2\mu_1\mu_2\cosh(2kH) + \left(\mu_1^2 + \mu_2^2\right)\sinh(2kH)}. \tag{58} $$

$$ \omega_2^v = -k\left(\gamma - \frac{A}{4k^2\pi H^4}\right) \frac{\mu_2[\cosh(2kH) - 1] + \mu_1[\sinh(2kH) - 2kH]}{\mu_2^2[\sinh(2kH) + 2kH] + 2\mu_1\mu_2\cosh(2kH) + \mu_1^2[\sinh(2kH) - 2kH]}. \tag{59} $$

Their dimensionless results will also be presented in Sec. II F.

F. Dimensionless solution

To provide the dimensionless form of each solution, we first define the dimensionless parameters:

$$ K = kH, \quad \beta = \frac{\mu_2}{\mu_1}, \quad \Omega_{\text{order}}^{\text{mode}} = \frac{\omega_{\text{order}}^{\text{mode}}\mu_1 H}{\gamma_1}, \quad \alpha = \frac{A}{\gamma_1 H^2}, \quad {}^{\text{mode}}\tilde{\eta}_{(i)}^* = \frac{{}^{\text{mode}}\tilde{\eta}_{(i)}}{H}, \tag{60} $$

where K represents the dimensionless wave number, β denotes the viscosity ratio, $\Omega_{\text{order}}^{\text{mode}}$ signifies the dimensionless growth rate, and α is used to characterize the ratio of van der Waals forces to surface tension. ${}^{\text{mode}}\tilde{\eta}_{(i)}^*$ represents the dimensionless amplitude of the perturbation.

The dimensionless results of the first-order dispersion relation are given as follows:

$$ \Omega_1^v = \frac{\alpha - \pi K^2}{2\pi K} \frac{\beta(\cosh(K) - 1) + \sinh(K) - K}{\beta^2[\sinh(K) + K] + 2\beta\cosh(K) + \sinh(K) - K}, \tag{61} $$

$$ \Omega_1^s = -\frac{K}{4} \frac{K + \beta + \beta\cosh(K) + \sinh(K)}{K(1 - \beta)(1 + \beta) + 2\beta\cosh(K) + (1 + \beta^2)\sinh(K)}. \tag{62} $$

Then the dimensionless results of the second-order dispersion relation are obtained as

$$\Omega_2^v = \frac{\alpha - 4\pi K^2}{4\pi K} \frac{\beta(\cosh(2K) - 1) + (\sinh(2K) - 2K)}{\beta^2[\sinh(2K) + 2K] + 2\beta\cosh(2K) + [\sinh(2K) - 2K]}, \tag{63}$$

$$\Omega_2^s = -\frac{K}{2} \frac{2K + \beta + \beta\cosh(2K) + \sinh(2K)}{2K(1-\beta)(1+\beta) + 2\beta\cosh(2K) + (1+\beta^2)\sinh(2K)}. \tag{64}$$

Finally, the dimensionless results of the second-order perturbation amplitude are given as follows:

$$\begin{aligned} {}^{22,vv}\tilde{\eta}_1^* = {} & \frac{4({}^{1,v}\tilde{\eta}_1^*)^2 \times \{\alpha[K + \beta - \beta\cosh(K) - \sinh(K)] \times [-2K - \beta + \beta\cosh(2K) + \sinh(2K)]}{[K - \beta\cosh(K) + \beta - \sinh(K)] \times \big\{\alpha(2K+\beta) - 4\pi K^2\big[2\pi + 4\Omega_1^v + \beta - 4\Omega_1^v\beta^2\big]} \\ & \frac{+ 2\pi K^3\beta\Omega_1^v \times [K(-2 + \beta + \beta^2) + 2\beta\cosh(2K) + (1+\beta^2)\sinh(2K)]\}}{+ \big[-\alpha + 4\pi K\big(K + 4\Omega_1^v\big)\big] \times \beta \times \cosh(2K)} \\ & + \big[-\alpha + 4\pi K\big(K + 2\Omega_1^v(1+\beta^2)\big)\big] \times \sinh(2K)\big\} \end{aligned} \tag{65}$$

$${}^{22,vv}\tilde{\eta}_1^* = -{}^{22,vv}\tilde{\eta}_2^*, \tag{66}$$

$$\begin{aligned} {}^{22,ss}\tilde{\eta}_1^* = {} & \frac{4e^{-2K}\pi({}^{1,s}\tilde{\eta}_1^*)^2K^3\Omega_1^s\beta \times [(-1+\beta^2) - e^{4K}(1+\beta)^2 - 2e^{2K}K(-2+\beta+\beta^2)]}{[K + \beta\cosh(K) + \beta + \sinh(K)] \times \big\{\alpha(2K+\beta) + 4\pi K^2[(2K+\beta) - 4\Omega_1^s(-1+\beta^2)]} \\ & + \big[\alpha - 4\pi K\big(K + 4\Omega_1^s\big)\big] \times \beta \times \cosh(2K) \\ & + \big[\alpha - 4\pi K\big(K + 2\Omega_1^s(1+\beta^2)\big)\big] \times \sinh(2K)\big\} \end{aligned} \tag{67}$$

$${}^{22,ss}\tilde{\eta}_1^* = -{}^{22,ss}\tilde{\eta}_2^*, \tag{68}$$

$$\begin{aligned} {}^{22,sv}\tilde{\eta}_1^* = {} & -\frac{2({}^{1,s}\tilde{\eta}_1^*)({}^{1,v}\tilde{\eta}_1^*)K^2\beta \times \big[\big(\Omega_1^s + \Omega_1^v\big)(K+\beta) - \big(\Omega_1^s - \Omega_1^v\big)(\beta\cosh(K) + \sinh(K))\big]}{[K + \beta - \beta\cosh(K) - \sinh(K)][K + \beta + \beta\cosh(K) + \sinh(K)]} \\ & \times [2K(2\beta^2 + 5\beta - 7) - 8\beta\cosh(2K) - (7\beta^2 - 6\beta + 7)\sinh(2K)], \\ & \times \big\{2K\big[8K + 5\big(\Omega_1^s + \Omega_1^v\big) + \big(4 + \Omega_1^s + \Omega_1^v\big)\beta - 6\big(\Omega_1^s + \Omega_1^v\big)\beta^2\big] \\ & + \big[8K + \big(\Omega_1^s + \Omega_1^v\big)(5\beta^2 - 2\beta + 5)\big]\sinh(2K) + 8\big(K + \Omega_1^s + \Omega_1^v\big)\beta\cosh(2K)\big\} \end{aligned} \tag{69}$$

$${}^{22,sv}\tilde{\eta}_1 = {}^{22,sv}\tilde{\eta}_2, \tag{70}$$

$${}^{21,vv}\tilde{\eta}_{(i)}^* = -{}^{22,ss}\tilde{\eta}_{(i)}^* - {}^{22,vv}\tilde{\eta}_{(i)}^*, \tag{71}$$

$${}^{21,ss}\tilde{\eta}_{(i)}^* = -{}^{22,sv}\tilde{\eta}_{(i)}^*, \tag{72}$$

$${}^{23,s\bar{s}}\tilde{\eta}_{(i)} = 0, \quad {}^{23,v\bar{v}}\tilde{\eta}_{(i)} = 0, \quad {}^{23,s\bar{v}}\tilde{\eta}_{(i)} = 0. \tag{73}$$

Based on the aforementioned results, it is apparent that the second-order perturbations resulting from the first-order varicose mode or the first-order sinuous mode belong to the varicose mode, and their combined effect with the first-order perturbation leads to the liquid sheet rupture. In contrast, the second-order perturbation generated by the simultaneous occurrence of both modes belongs to

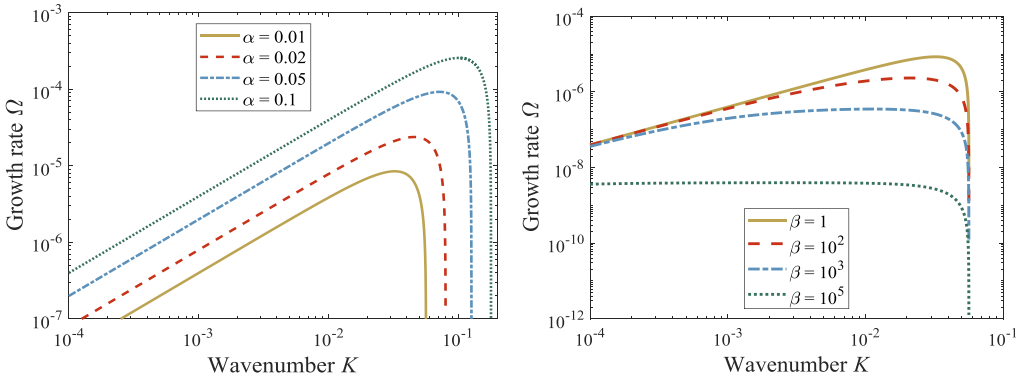

FIG. 2. Dispersion relation of the first-order varicose mode. (a) Considering the influence of different values of parameter α (symbolizing the dimensionless ratio of van der Waals force to surface tension), where $\beta = 1$. (b) Considering the influence of different viscosity ratios β, with parameter $\alpha = 0.01$.

the sinuous mode, which does not contribute directly to the liquid sheet rupture. The dispersion relation of the second-order growth rate resulting from the varicose mode is in agreement with that of the sinuous mode.

III. RESULTS AND DISCUSSION

The linear stability of the viscous fluid with a nanoscale thickness has been studied previously by researchers. Liang [35] and Xu [33] have both investigated its linear stability, with the latter focusing on the case of multiple liquid layers and verifying the model using a three-layer scenario where the first and third layers are identical. The comparison between Eqs. (33) and (59) with the results obtained by Xu shows consistent findings.

Next, the first-order and second-order outcomes will be presented and the influence of the parameter α and viscosity ratio β on the outcomes will be explored. Furthermore, the contribution of each component to the sheet rupture will be compared in this section.

A. The first-order results

The solution for the first-order results has been obtained in Sec. II D. The dispersion relation ω_1^v for the first-order stretching mode is given by Eq. (33). Its dimensionless result Ω_1^v is provided by Eq. (61). This represents the growth rate of perturbations, which provides the maximum perturbation growth rate $\Omega_{1,\max}^v$ as it varies with the dimensionless wave number K. The corresponding wave number is considered the dominant or most important wave number ($K_{\max}$) as it records the highest growth rate [36]. The dispersion relation of the first-order sinuous mode and its dimensionless form are also given in Eqs. (35) and (62), respectively.

The Fig. 2 shows the dispersion relation of the first-order varicose mode, taking into account the effect of α and viscosity ratio on the dispersion relation. The dispersion relations for different values of α are presented in Fig. 2(a), with a constant viscosity ratio $\beta = 1$. Figure 2(b) shows the dispersion relation for different viscosity ratios, with a constant α value. As shown in Fig. 2(a), it can be observed that the growth rate Ω_1^v increases first and then decreases as the wave number increases. Moreover, when the wave number becomes sufficiently large, the growth rate becomes negative, indicating that the disturbance will not increase with time, but will decay over time. At this point, the liquid sheet is stable. Meanwhile, it can also be observed from Fig. 2(a) that as α increases, which indicating a strengthening of van der Waals force, the maximum growth rate

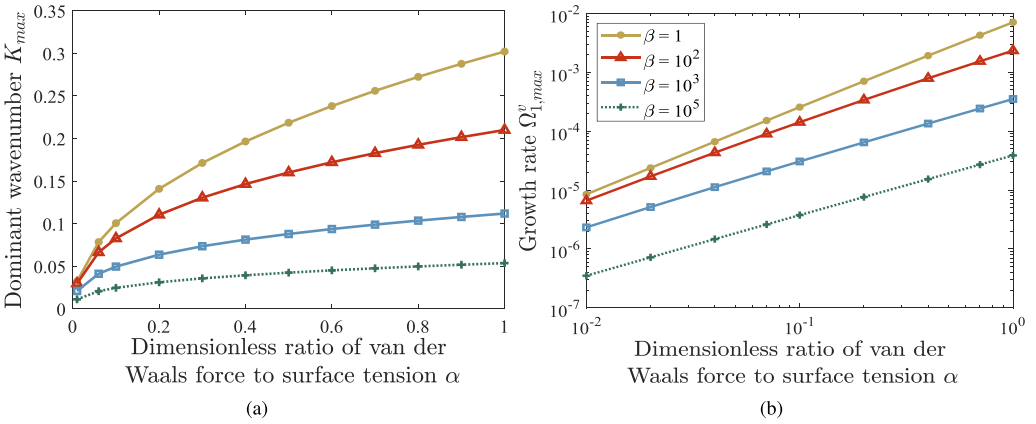

FIG. 3. The influence of the parameter α (symbolizing the ratio of van der Waals force to surface tension) and viscosity ratio β on the maximum growth rate $\Omega^v_{1,\max}$ and dominant wave number $K_{\max}$ of perturbations under varicose mode. (a) Influence on dominant wave number. (b) Influence on maximum growth rate.

increases, and the dominant wave number also increases. This is because the van der Waals force act as intermolecular force and exhibit intermolecular attraction at the nanoscale. Moreover, the closer the distance between molecules, the stronger the attraction between them. Therefore, in varicose mode, the attractive force between the thinner regions between two interfaces is larger than that between thick regions. This leads to a decrease in the thickness of the originally thinner regions, making them more unstable. As a result, the strengthening of van der Waals force increases the growth rate of the disturbance. On the other hand, the effect of viscosity is opposite to that of α. As shown in Fig. 2(b), when the viscosity ratio increases, which mean the viscosity of the intermediate liquid layer is greater, the maximum growth rate decreases and the corresponding dominant wave number decreases. This indicates that an increase in the viscosity of the liquid sheet enhances its stability. This is because its viscosity impedes the development of disturbances, making it more difficult for disturbances to grow, and thus making the system more stable.

The effects of the parameter α and viscosity ratio β on the maximum growth rate $\Omega^v_{1,\max}$ and the corresponding dominant wave number $K_{\max}$ of the first-order varicose mode are better illustrated in Fig. 3. It can be clearly seen from Fig. 3 that, as α increases, both the maximum growth rate and the corresponding dominant wave number increase. In contrast, as the viscosity ratio β increases, both the maximum growth rate and the corresponding dominant wave number decrease. These observations are consistent with the information presented in Fig. 2.

Figure 4 shows the dispersion relation of the first-order sinuous mode. From Eq. (62), it is evident that the dispersion relation of the first-order sinuous mode is independent of α. This can be easily explained by the fact that the thickness of the liquid sheet remains constant under the sinuous mode, and thus the magnitude of the van der Waals forces between the upper and lower layers of the sheet is uniform. Therefore, the magnitude of the van der Waals forces does not affect the growth rate of the first-order sinuous mode. As can be seen from Fig. 4, when the viscosity ratio $\beta = 1$, the growth rate continuously decreases with increasing wave number. In cases of higher viscosity ratios, although the growth rate exhibits a brief recovery, it subsequently continues to decrease and remains negative, indicating that the liquid sheet is stable under small perturbations. This is because both surface tension and viscosity have a dampening effect on the perturbation to enhance the stability of the liquid sheet [6]. Furthermore, Fig. 4 also reveals that, for large wave number under the sinuous mode, the maximum growth rate is minimized when the viscosity ratio $\beta = 1$, indicating that the liquid sheet is most stable in this state.

Furthermore, by comparing the results in Fig. 4 with Fig. 2(b), it can be observed that $\Omega^v_{1,\max} + \Omega^s_{1,\max}$ is always a negative value, which implies that the $\exp(\omega^s_1 t + \omega^v_1 t + 2ikz)$ term generated

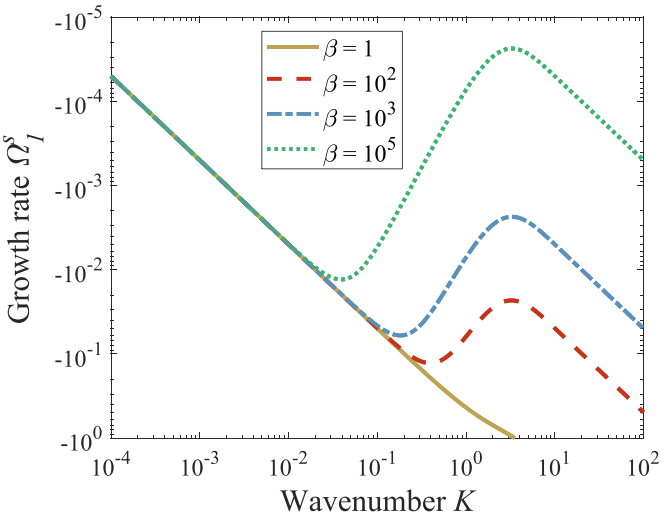

FIG. 4. The dispersion relation under sinuous mode.

by the coupling of the two modes is also a stabilizing term. It has almost no contribution to the development of perturbations and the breakup of the liquid sheet.

B. The second-order results

The dominant wave number selected from the linear analysis results is chosen as the characteristic wave number for the second-order analysis [16]. The rationality of choosing $K_{1,\max}$ (the first-order dominant wave number) as the dominant wave number instead of $K_{2,\max}$ (the second-order dominant wave number) will be explained in Appendix. A. Using Eqs. (33) and (35), we can calculate the growth rates, ω_1^v and ω_1^s, for the varicose and sinuous modes, respectively. Additionally, utilizing Eqs. (58) and (59), we can calculate the second-order growth rates, ω_2^v and ω_2^s, for the two modes, respectively. It should be noted that the superscripts in this context refer to first-order perturbation modes and not second-order modes. Furthermore, we can obtain the magnitudes of each perturbation amplitude from Eqs. (65)–(73). Finally, substituting all of these results into Eqs. (37) and (44) yields the expression (74) for the surface waves of the liquid sheet, where the subscript "(i)" takes on the value of 1 or 2 to indicate the lower or upper interface, respectively:

$$\begin{aligned} Y_{(i)} = \bar{Y}_{(i)} &+ {}^{1,s}\tilde{\eta}_{(i)} \exp\left(\omega_1^s t + ikz\right) + {}^{1,v}\tilde{\eta}_{(i)} \exp\left(\omega_1^v t + ikz\right) \\ &+ {}^{21,ss}\tilde{\eta}_{(i)} \exp\left(\omega_2^s t + 2ikz\right) + {}^{21,vv}\tilde{\eta}_{(i)} \exp\left(\omega_2^v t + 2ikz\right) \\ &+ {}^{22,ss}\tilde{\eta}_{(i)} \exp\left(2\omega_1^s t + 2ikz\right) + {}^{22,vv}\tilde{\eta}_{(i)} \exp\left(2\omega_1^v t + 2ikz\right) \\ &+ {}^{22,sv}\tilde{\eta}_{(i)} \exp\left(\omega_1^s t + \omega_1^v t + 2ikz\right). \end{aligned} \tag{74}$$

From the analysis in Sec. III A, we have learned that the term ${}^{22,sv}\tilde{\eta}_{(i)} \exp(\omega_1^s t + \omega_1^v t + 2ikz)$ tends towards stability. In fact, the disturbance it causes can be considered negligible.

Based on the analysis in Sec. III A, it can be seen that the primary mode causing instability of the liquid sheet is the first-order varicose mode. The surface waveform is given by Eq. (75) when the first-order mode is varicose:

$$Y_{(i)} = \bar{Y}_{(i)} + {}^{1,v}\tilde{\eta}_{(i)} \exp\left(\omega_1^v t + ikz\right) + {}^{21,vv}\tilde{\eta}_{(i)} \exp\left(\omega_2^v t + 2ikz\right) + {}^{22,vv}\tilde{\eta}_{(i)} \exp\left(2\omega_1^v t + 2ikz\right). \tag{75}$$

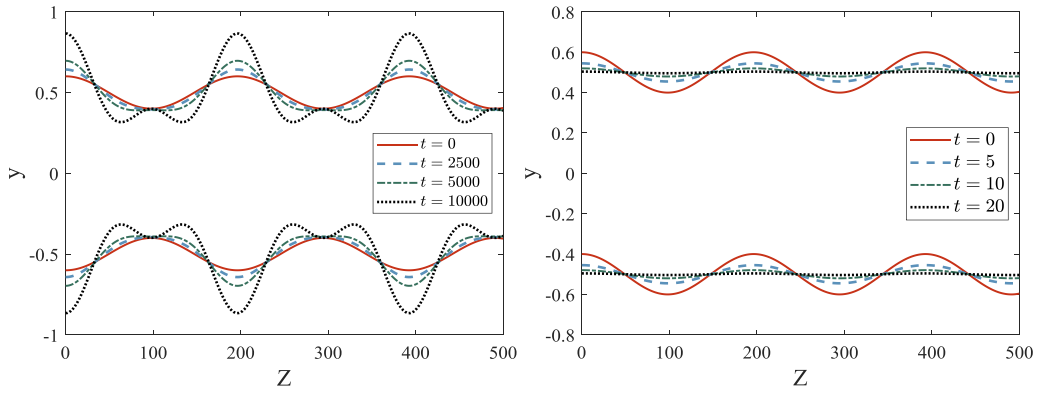

FIG. 5. Surface wave profile in the liquid sheet. (a) Varicose mode. (b) Sinuous mode. The parameters are set as follows: the dimensionless ratio of van der Waals forces to interfacial tension $\alpha = 0.010$, non-dimensional initial disturbance ${}^{1}\tilde{\eta}_1^* = 0.1$, and viscosity ratio $\beta = 1$.

For the surface shape when the first-order mode is sinuous, it is given by

$$Y_{(i)} = \bar{Y}_{(i)} + {}^{1,s}\tilde{\eta}_{(i)} \exp\left(\omega_1^s t + ikz\right) + {}^{21,ss}\tilde{\eta}_{(i)} \exp\left(\omega_2^s t + 2ikz\right) + {}^{22,ss}\tilde{\eta}_{(i)} \exp\left(2\omega_1^s t + 2ikz\right). \quad (76)$$

Similarly, the ratio of thickness is used to nondimensionalize Y and z as $y = Y_{(i)}/H$ and $Z = z/H$. It is noteworthy that in the present section, the dimensionless forms will be employed for the purpose of discussing the obtained results in a rigorous manner.

First, determine which mode dominates. Utilizing the dimensionless form of Eqs. (75) and (76), the shapes of the liquid sheet under the first-order varicose mode and the first-order sinuous mode are drawn separately, as shown in Fig. 5. Figure 5(a) shows the result under the first-order varicose mode, while Fig. 5(b) shows the result under the first-order sinuous mode. The dimensionless ratio of van der Waals forces to interfacial tension is set to $\alpha = 0.010$. For comparison purposes, the dimensionless first-order perturbations under both modes are set to $\tilde{\eta}_1^* = 0.1$, which mean it is $1/10$ of the sheet thickness. The viscosity ratio is set to $\beta = 1$. From Fig. 5(a), it can be seen that the liquid sheet still shows linear results when the time is not long enough. The perturbations have not fully developed yet. As time increases, the perturbations on the liquid sheet surface continue to increase, and the nonlinear effects are very obvious. It can be anticipated that if the liquid sheet ruptures, they will exhibit an alternating arrangement of thick and thin threads. This phenomenon has also been observed in the nonlinear stability analysis of power-law fluids with consideration only of the varicose mode by previous researchers [37]. Under the varicose mode, the perturbations on the liquid sheet surface continue to grow. However, as presented in Fig. 5(b), the sinuous mode exhibits negative growth rate, rendering it stable with a considerably short period for achieving stability. As a result, the varicose mode, even if it appears as second-order perturbations, barely affects the rupture of the liquid sheet. Hence, in assessing the rupture of the liquid sheet, the influence of the first-order sinuous mode can be largely discounted.

Second, the influence of each parameter on the surface wave was investigated. Considering the first-order mode primarily as a varicose mode, taking the maximum value of $K_{1,\max}$ as the primary wave number, the surface shape is determined solely by Eq. (75). Using this equation, the effect of the dimensionless ratio of van der Waals forces to interfacial tension α and viscosity ratio β on the surface shape is studied, as shown in Fig. 6. Specifically, Fig. 6(a) illustrates the liquid sheet shapes at different α values with a viscosity ratio of $\beta = 1$ at the same instant. Meanwhile, Fig. 6(b) demonstrates the effect of different viscosity ratios β on the liquid sheet shape at the same time, with $\alpha = 0.01$. The dimensionless initial perturbation of the first order is set to ${}^{1,v}\tilde{\eta}_1^* = 0.1$. Observing Fig. 6(a), it is evident that the perturbations in the liquid sheet develop more rapidly

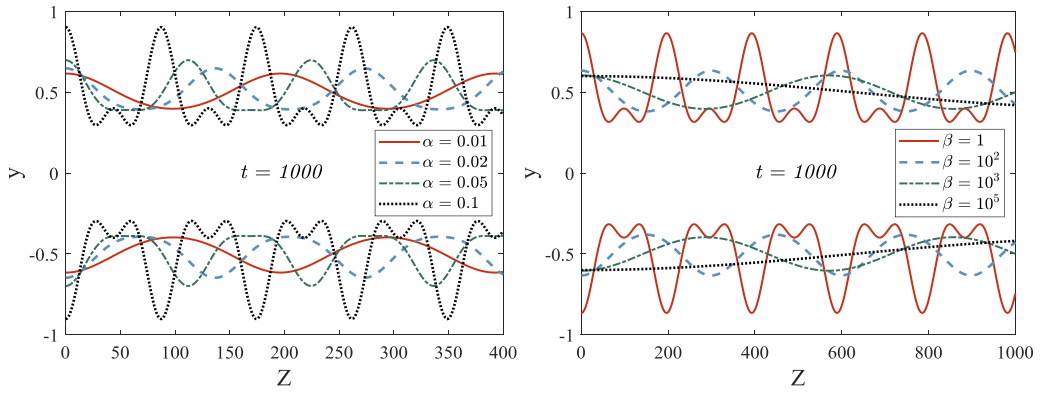

FIG. 6. Effects of various parameters on liquid sheet shape. (a) Effect of the dimensionless ratio of van der Waals forces to interfacial tension α on liquid sheet shape, with viscosity ratio $\beta = 1$. (b) Effect of viscosity ratio β on liquid sheet shape, with parameter $\alpha = 0.01$. The dimensionless initial first-order perturbation is ${}^{1}\tilde{\eta}_1^* = 0.1$.

with increasing values of α. This observation aligns with our prior analyses. Additionally, an increase in the dimensionless ratio of van der Waals forces to interfacial tension α leads to a larger dominant wave number, resulting in smaller characteristic wavelengths of the surface waves, as clearly demonstrated in Fig. 6(a). Conversely, from Fig. 6(b), we can observe that the amplitude of the liquid sheet disturbance is greater with a lower viscosity ratio at a given time. This finding is consistent with our earlier analysis indicating that a higher viscosity ratio improves the stability of the liquid sheet. Furthermore, we can also observe from Fig. 6(b) that larger characteristic wavelengths of the surface waves correspond to a greater viscosity ratio, consistent with our prior analysis that the dominant wave number decreases with an increasing viscosity ratio. The results shown in Fig. 6 indicate that, to achieve a smaller liquid column diameter, there are two approaches. First, one can increase the α, which can be achieved by using materials with a larger Hamaker constant or a smaller surface tension coefficient, or by reducing the thickness. Second, a smaller liquid column diameter can also be achieved by making the viscosity ratio between the liquid sheet and the outer fluid closer to 1.

Third, the contribution of the first-order and second-order terms to the breakup of the liquid sheet was investigated. The impact of various parameters on the shape of the liquid sheet has been discussed. However, the actual contribution of the second-order perturbations to the process of liquid sheet rupture remains unclear. Therefore, to facilitate a better comparison between the development of first-order and second-order waves, they are separated and plotted on the same graph, as shown in Fig. 7. The dimensionless ratio of van der Waals forces to interfacial tension is $\alpha = 0.01$, with a dimensionless initial first-order perturbation of ${}^{1,v}\tilde{\eta}_1^* = 0.1$. Figure 7(a) reveals that the initial waves are primarily first order. At this stage, the magnitude of second-order waves is relatively small, and their half wavelength is distinct from that of the first-order waves, consistent with previous analysis. Subsequently, Figs. 7(b)–7(d) illustrate the increasing amplitude of second-order waves over time and their rising proportion of the entire wave, indicating their eventual dominance. These results clarify why linear analysis is inadequate in predicting the development of perturbations and the shape of liquid sheets over extended periods.

The ramifications of second-order waves are of paramount importance and may even outstrip those of first-order waves. According to Eq. (75), the second-order waves can be decomposed into two distinct components: the first is the inherent second-order wave, while the second is the transmission of the first-order wave to the second order. Figure 8 depicts the contributions of the two distinct components in second-order waves. The dimensionless ratio of van der Waals forces

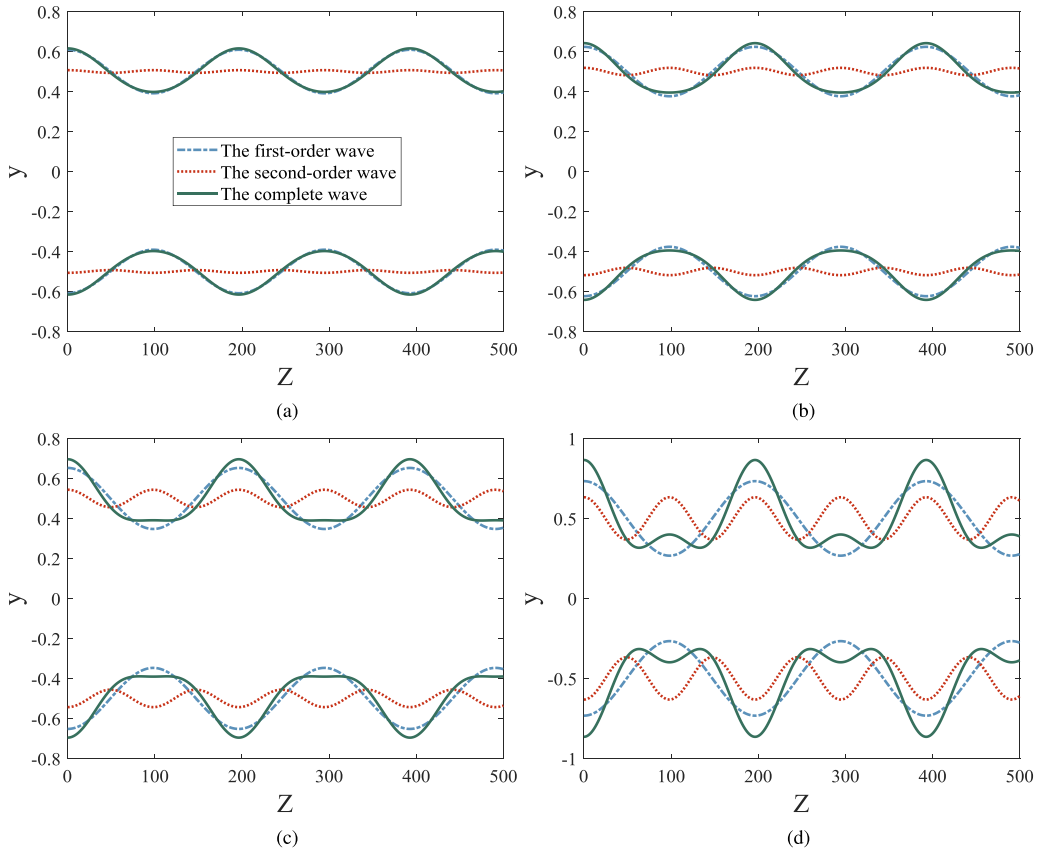

FIG. 7. Waveform evolution: (a) $t = 1000$, (b) $t = 2500$, (c) $t = 5000$, (d) $t = 10\,000$. Comparison of the development of first-order and second-order waves and their contributions to liquid sheet rupture. The parameters are $\alpha = 0.010$, ${}^{1}\tilde{\eta}_1^* = 0.1$, and $\beta = 1$.

to interfacial tension α is assigned a value of $\alpha = 0.01$. And the dimensionless initial first-order disturbance is initialized to ${}^{1,v}\tilde{\eta}_1^* = 0.1$. An examination of Fig. 8(a) reveals that, in the short term, the amplitudes of the inherent second-order wave and the first-order-to-second-order transmitted wave are reasonably comparable, though with a phase difference of a half cycle. However, over time, Figs. 8(b) to 8(d) indicate that the first-order-to-second-order transmitted wave becomes increasingly dominant, with an amplitude far greater than that of the inherent second-order wave. Consequently, it can be deduced that the primary contributor to second-order waves is the first-order-to-second-order transmitted wave.

At this stage, an essentially complete analysis has been conducted regarding the relative contributions of various waves to the breakdown of the liquid sheet. Second-order perturbations make a significant contribution to the development of surface waves on the liquid sheet. Within the realm of second-order waves, the first-order-to-second-order transmitted wave has been shown to play a primary role. In fact, this observation can be aptly explained with reference to Eq. (75) and the preceding analytical results. Due to the faster development of the perturbation when $K_{1,\max}$ is chosen as the primary wave number, it was selected for analysis. The second-order growth rate Ω_2^v at $K_{1,\max}$ is found to be significantly small or even negative, suggesting that it tends towards stability. Consequently, the first-order-to-second-order transmitted wave ${}^{22,vv}\tilde{\eta}_{(i)} \exp(2\omega_1^v t + 2ikz)$ is dominant in second-order waves. Meanwhile, the first-order wave is ${}^{1,v}\tilde{\eta}_{(i)} \exp(\omega_1^v t + ikz)$. Specifically, for ${}^{22,vv}\tilde{\eta}_{(i)} \exp(2\omega_1^v t + 2ikz)$, the growth rate is $2\omega_1^v$. In contrast, for ${}^{1,v}\tilde{\eta}_{(i)} \exp(\omega_1^v t + ikz)$, the growth

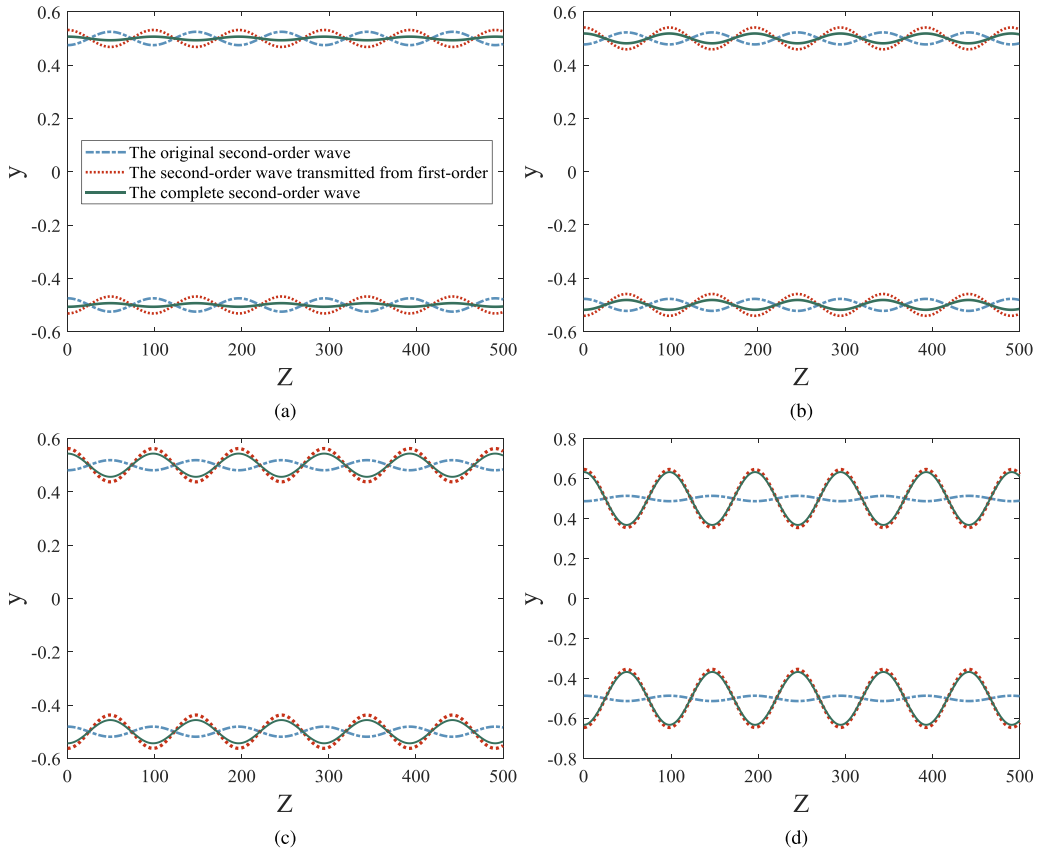

FIG. 8. Waveform evolution of second-order waves: (a) $t = 1000$, (b) $t = 2500$, (c) $t = 5000$, (d) $t = 10\,000$. Comparison of the contributions of the original second-order waves and the first-order waves transmitted to second order to liquid sheet rupture. The parameters are $\alpha = 0.010$, ${}^{1}\tilde{\eta}_1^* = 0.1$, and $\beta = 1$.

rate is ω_1^v. The growth rate of the second-order perturbation is two times higher than that of the first-order perturbation. Thus, under minimal initial amplitude of the second-order perturbation, the relatively large growth rate can facilitate its gradual development and even surpass that of the first-order wave.

Finally, the influence of different values of the ratio of van der Waals forces to interfacial tension α and viscosity ratio β on the second-order initial amplitude ${}^{22,vv}\tilde{\eta}_1^*$ was investigated. The first-order initial perturbation was fixed at ${}^{1,v}\tilde{\eta}_1^1 = 0.1$. Four distinct viscosity ratios β (1, 10, 10^2, 10^3) were considered for comparative analysis. The outcomes are illustrated in Fig. 9, indicating a slight reduction in the second-order initial amplitude with an increase in α, albeit with limited magnitude. Thus, a smaller initial amplitude may still lead to a faster evolution of disturbances due to a heightened growth rate. Conversely, an escalation in viscosity ratio is found to cause a reduction in the second-order initial amplitude. In previous analyses, this increase was shown to cause a decrease in the growth rate. Therefore, a higher viscosity ratio will exert an adverse impact on the liquid sheet's instability, substantially increasing its rupture time.

It is noteworthy that the cross-sectional area of the liquid thread after the sheet breakup can be controlled by adjusting the initial perturbation and sheet thickness. This provides valuable insights for the manufacture of nanowires. This aspect will be elaborated in the subsequent section.

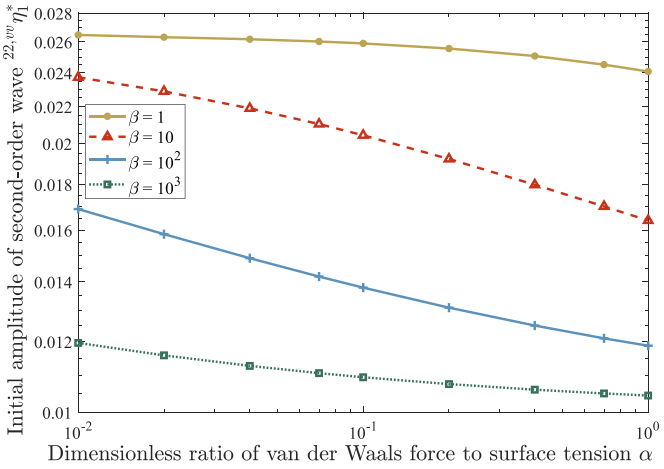

FIG. 9. The effects of the ratio of van der Waals forces to interfacial tension α and viscosity ratio β on the initial amplitude of second-order waves. The dimensionless initial first-order perturbation is $^1\tilde{\eta}_1^* = 0.1$.

IV. APPLICATIONS IN FIBER THERMAL DRAWING

In recent years, a growing body of literature has examined the use of thermal stretching methods in the production of nanowires or fibers with nanostructures. During this process, a macroscopic multimaterial structure, referred to as a "preform," is subjected to heating and subsequent stretching, reducing it to microscale transverse dimensions [28,30,33,38,39]. Although stretching is not considered in this model, the liquid sheet in this model can be regarded as the state of the sheet after being stretched in the "preform." It is assumed that the sheet has reached its thinnest point due to stretching. Therefore, the theoretical analysis results presented earlier in this paper can provide a theoretical basis for stability analysis in the control of nanowire dimensions. Moreover, these theoretical analysis can provide more guidance for a broader range of applications.

In the following analysis, we consider a commonly used PES/As_2Se_3/PES multilayer composite material. The relevant parameters for this material are as follows: the surface tension coefficient $\gamma = 0.1$ Nm^{-1}, the liquid sheet viscosity $\mu = 10^5$ Pa s, and the viscosity ratio $\beta = 1$. The Hamaker constant is set to $A = 10^{-17}$ J.

A. Nanowire size prediction

The schematic diagram of the liquid filaments patterns after the liquid film rupture is illustrated in Fig. 10. The filament after rupture consists of both main filaments and satellite filaments. This phenomenon was also observed by Esposito [30].

In fact, the second-order weak nonlinear stability analysis cannot accurately predict the conditions at the moment of breakup considering the strong nonlinear evolution at late stages of the

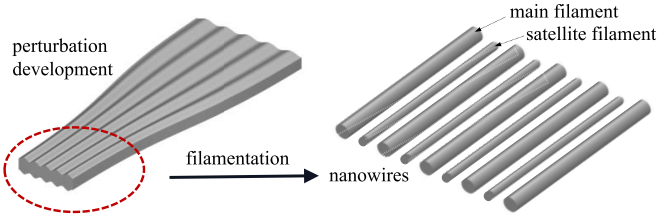

FIG. 10. Schematic diagram of filamentation.

TABLE I. Ratio of main to satellite liquid filament diameters D_m/D_s.

	The sheet thickness H (nm)				
${}^1\tilde{\eta}_1$ (nm)	100	80	60	40	20
2	1.9163	1.9208	1.9390	1.9376	1.9841
4	1.9174	1.9211	1.9414	1.9491	2.0588
6	1.9187	1.9244	1.949	1.9761	2.2339
8	1.9225	1.9320	1.9618	2.0233	2.3393
10	1.9280	1.9427	1.9835	2.0938	3.1701

instability. We can still use the theoretical results obtained in this study, selecting the liquid film configuration close to the breakup moment, to estimate the diameter of the filaments post-breakup, like using the wavelength of the most dangerous perturbation to estimate the droplet diameter in a linear stability analysis. Therefore, we temporarily choose to use the shape of the liquid film just before rupture to calculate the diameters of the liquid filaments. A time step of 10^{-3} is chosen, and the spatial step is set to 2.5×10^{-4} times the wavelength of the perturbation. The previous time step when the upper and lower interfaces intersect is chosen as the moment of rupture. Then, we use the liquid film shape at the moment of rupture to calculate the cross-sectional areas of the regions forming the main filament and the regions forming the satellite filament. This is done by integrating these areas separately using the Newton-Raphson method, resulting in the cross-sectional areas, denoted as A_m and A_s, for the main and satellite filaments, respectively. And the liquid filaments will transform into cylindrical shapes under the action of surface tension, allowing for the calculation of the diameter of the cylindrical liquid filaments directly. In this context, $D_m = 2 \times \sqrt{A_m/\pi}$ refers to the diameter of the main liquid filament, while $D_s = 2 \times \sqrt{A_s/\pi}$ denotes the diameter of the satellite liquid filament. This paper focuses on the ratio of the diameter between the main liquid filament and the satellite liquid filament, which is denoted as D_m/D_s. The specific data regarding the filament diameters are included in Appendix B.

In total, five distinct liquid sheet thicknesses were employed (100, 80, 60, 40, 20 nm), alongside five different initial disturbance amplitudes ${}^1\tilde{\eta}_1$ (2, 4, 6, 8, 10 nm).

In the obtained results, the diameter of the main liquid filament is primarily determined by the sheet thickness. Regarding the diameter ratio between the main and satellite liquid filaments, when the ratio of the initial disturbance amplitude to the thickness is less than 0.1, which is written as ${}^1\tilde{\eta}_1/H < 0.1$, the diameter ratio of the main to satellite liquid threads, D_m/D_s, is approximately constant, ranging from 1.91 to 1.94. However, when this ratio exceeds 0.1, the magnitude of the initial disturbance amplitude has a marked effect on the ratio D_m/D_s. This effect is especially notable when the thickness is small and the disturbance is large, which is exemplified by the data in Table I. When $H = 20$ nm and ${}^1\tilde{\eta}_1 = 10$ nm, the value of D_m/D_s in this case exceeds 3. This result is likely attributed to the insufficient development of the second-order perturbation at that stage. As the growth rate of the second-order perturbation is greater, its contribution becomes more significant over time. However, in the case of large perturbations and small sheet thickness, the second-order perturbation has not had sufficient time to fully develop before sheet rupture occurs. Therefore, in such scenarios, the dominant role in sheet rupture is played by the first-order perturbation. Consequently, the results obtained under these conditions differ significantly from those observed after the full development of the second-order perturbation. A more detailed explanation is provided in Appendix C.

The influence of the liquid sheet thickness H and the initial perturbation amplitude ${}^1\tilde{\eta}_1$ on the diameter ratio of the liquid filaments is presented in Fig. 11. The smaller thickness and larger disturbance result in a larger ratio of diameter, and when ${}^1\tilde{\eta}_1/H > 0.1$ the increasing trend of this ratio becomes more pronounced. This information provides guidance for nanowire production, wherein control of the thickness of the liquid sheet can enable the desired diameter of main liquid

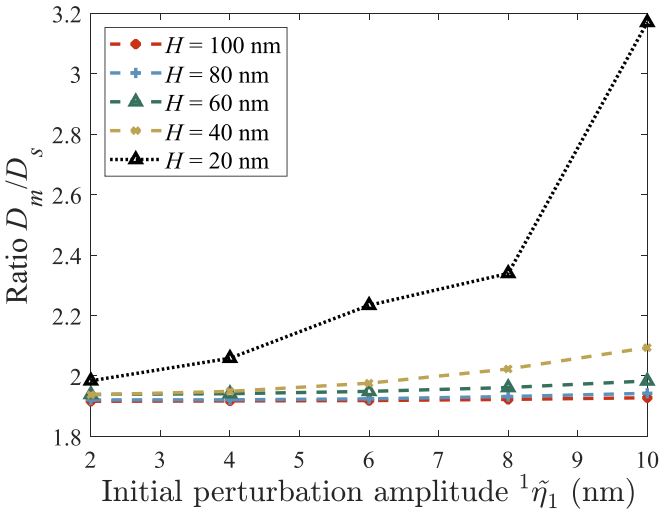

FIG. 11. The influence of liquid sheet thickness and initial perturbation on the diameter ratio between the main filament and the satellite filament.

filaments, while the ratio D_m/D_s can be controlled by regulating the initial disturbance amplitude to liquid sheet ratio. Therefore, to achieve a relatively stable size ratio, it is advisable to appropriately reduce the initial perturbation amplitude.

The above analysis indicates that the diameter of the liquid filaments D_m and D_s can be controlled by adjusting the thickness of the liquid sheet H and applying specific perturbations.

B. Controlled instability: Arbitrary small perturbations versus specific perturbations

In the study by Esposito *et al.* [30], the textured pattern was employed to control the instability in thermal drawing, where the roughness was regarded as arbitrary small initial perturbations ${}^1\tilde{\eta}_{\text{initial}}$ and the textured pattern as specific perturbations ${}^1\tilde{\eta}_T$ with their amplitude ratio ${}^1\tilde{\eta}_T^*/{}^1\tilde{\eta}_{\text{initial}}^* = 100$. Our nonlinear stability model is used to thoroughly study the controlled instability, by comparing the evolution of arbitrary small initial perturbations and specific ones. Here, we denote the dimensionless initial perturbation amplitude introduced by roughness as ${}^1\tilde{\eta}_{\text{initial}}^* = {}^1\tilde{\eta}_{\text{initial}}/H$, and the dimensionless amplitude of the applied specific perturbation as ${}^1\tilde{\eta}_T^* = {}^1\tilde{\eta}T/H$. The amplitude ratio is also set to be ${}^1\tilde{\eta}_T^*/{}^1\tilde{\eta}_{\text{initial}}^* = 100$. The wave number of the initial perturbation is chosen as $K_{1,\max}$ since perturbations at this frequency are the most likely to develop and grow rapidly. On the other hand, the wave number of the specific perturbation can be set artificially.

Here, we set ${}^1\tilde{\eta}_{\text{initial}}^* = 0.003$, which results in ${}^1\tilde{\eta}_T^* = 0.3$. The thickness of the liquid sheet is assumed to be $H = 50$ nm first. In the first case, the wave number of the specific perturbation is set as $k_T = 0.5 \times 10^6$ m^{-1}. Surface wave patterns of the two perturbations after their development are plotted, as shown in Figs. 12(a) and 12(b). It can be observed that when the specific perturbation reaches sheet rupture, the initial perturbation exhibits minimal growth. This suggests that the influence of roughness can be considered negligible. However, the wave number of the specific perturbation can be adjusted artificially. Therefore, when the wave number is modified to result in a significantly reduced growth rate of the specific perturbation, both disturbances can cause sheet rupture almost simultaneously. In the second case, by altering the wave number of the specific perturbation, such as $k_T = 8 \times 10^4$ m^{-1}, the arbitrary perturbations will also undergo significant development when specific perturbations are fully developed, as shown in Figs. 12(c) and 12(d). Thus, at certain wave number, the influence of roughness is negligible, and in this case the specific perturbations applied can be considered effective.

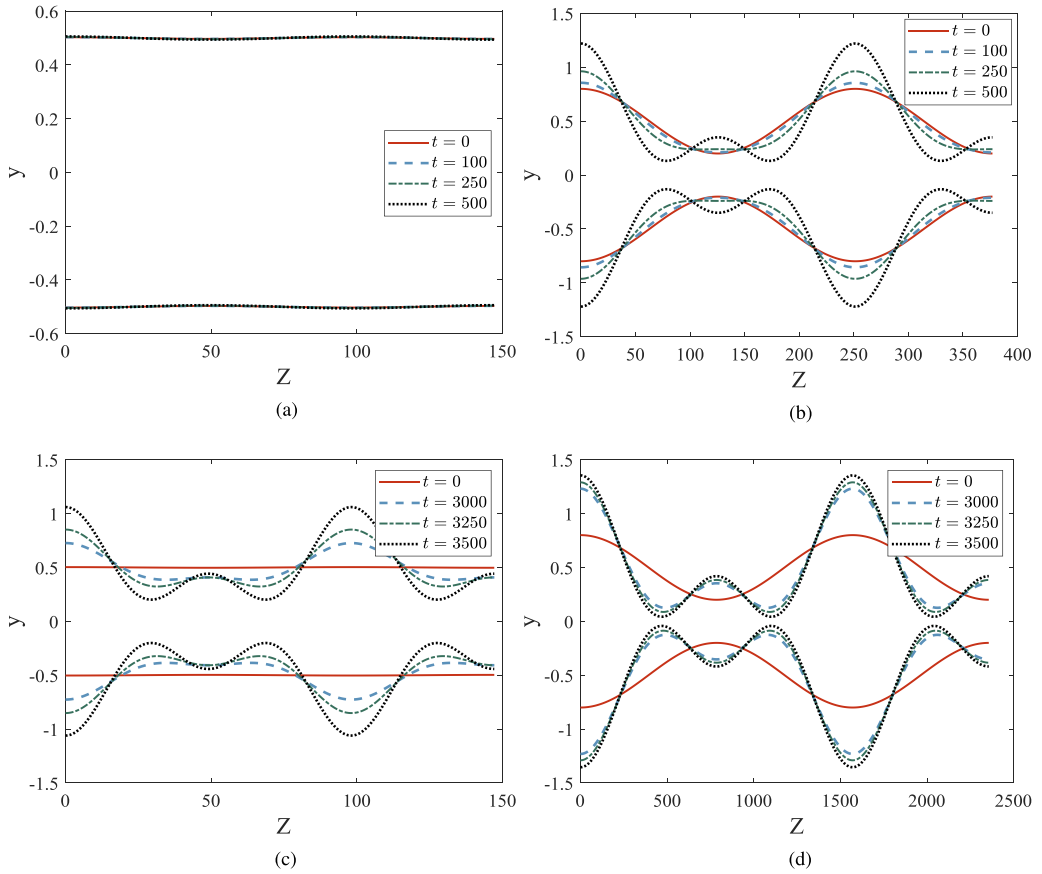

FIG. 12. The development of arbitrary small initial perturbations and specific perturbations. (a) In the first case, the development of arbitrary small initial perturbations. (b) In the first case, the development of specific perturbations. (c) In the second case, the development of arbitrary small initial perturbations. (d) In the second case, the development of specific perturbations.

Therefore, in this study, we consider that when specific perturbations have developed close to rupture, the amplitudes of perturbations that develop thereafter remain less than one-tenth of the thickness. This implies that the influence of roughness can be neglected. It should be noted that second-order nonlinear stability analysis cannot accurately predict the rupture of the liquid sheet, so this study is primarily exploratory in nature. In reality, as the liquid sheet approaches rupture, strong nonlinear effects accelerate the rupture, meaning that the actual rupture time is shorter than calculated here. Consequently, the development of weak perturbations is even smaller, justifying the reasonable assumption made here that the influence of roughness can be neglected. At this point, the wave number of the specific perturbation can be regarded as the effective wave number, defined as k_e. The upper and lower bounds of the effective wave number are two critical wave numbers, defined as $k_{c,\text{large}}$ and $k_{c,\text{small}}$, respectively. Changing the sheet thickness and the initial amplitude of the specific perturbation will also change the effective wave-number range.

The effective wave-number range obtained under different sheet thicknesses and specific perturbation initial amplitudes are presented in Table II. The results of the critical wave number are shown in Fig. 13. It can be seen that, for the same sheet thickness, a larger initial perturbation amplitude results in a larger effective wave-number range, because $k_{c,\text{large}}$ remains nearly constant, while $k_{c,\text{small}}$ decreases as the initial perturbation amplitude increases. The change in sheet thickness

TABLE II. The effective wave number k_e (10^4 m^{-1}).

	The sheet thickness H (nm)				
${}^1\tilde{\eta}_1$ (nm)	10	20	30	50	100
0.3	223–5434	60.6–1363	27.70–606.2	10.24–218.45	2.608–54.62
0.2	303–5321	82.3–1337	37.56–594.9	13.87–214.3	3.529–53.64
0.1	440–5160	118.9–1299	54.15–578.8	19.97–208.6	5.072–52.23

leads to a significant change in the critical wave number, with thicker sheets resulting in smaller critical wave number. It should be noted that the variation in thickness leads to changes in the dimensionless ratio of van der Waals force to surface tension α. This implies that the van der Waals forces undergo changes, and, as the thickness increases, the promoting effect of van der Waals forces on perturbation development becomes less significant

C. Fibers with nanostructures

We can fabricate fibers with different nanostructures by controlled instability through thermal drawing. First, if the middle layer liquid sheet is ruptured, fibers with self-assembled nanowires can be obtained [30]. As explained in Secs. IV A and IV B, we could predict the diameters of nanowires in the fiber and provide the effective wave-number range of specific perturbations when textured pattern applied to control the instability.

Second, if the middle layer liquid sheet is not yet broken in cross section, we can get fibers with sophisticated nanastructures. As shown in Fig. 14, it is observed that specific shapes of devices can be formed by applying specific perturbations and controlling the development time. Moreover, we can also modify the perturbation amplitudes or wave numbers of the two modes of perturbations to alter the obtained nanostructures in the fiber. In fact, we have obtained numerous different nanostructures, and Fig. 14 serves as an illustrative example. This implies that a wide variety of possibilities can be provided for functional devices in a single fiber, thereby presenting intriguing potential applications in practical engineering scenarios.

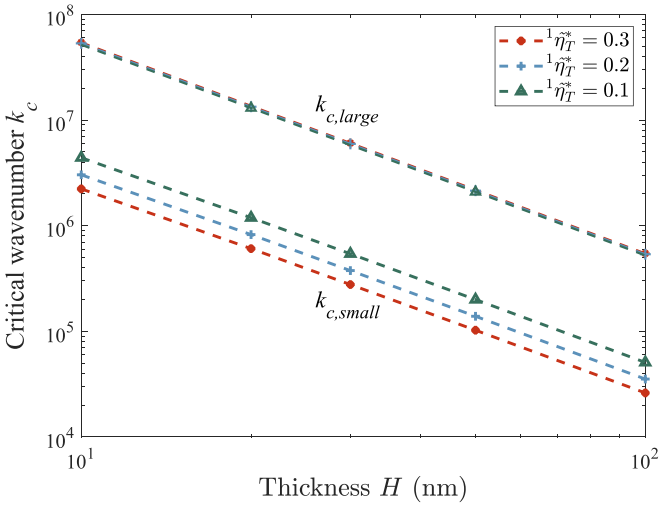

FIG. 13. The influence of the initial amplitude of perturbation ${}^1\tilde{\eta}_T^*$ and sheet thickness H on the critical wave numbers $k_{c,\text{large}}$ and $k_{c,\text{small}}$.

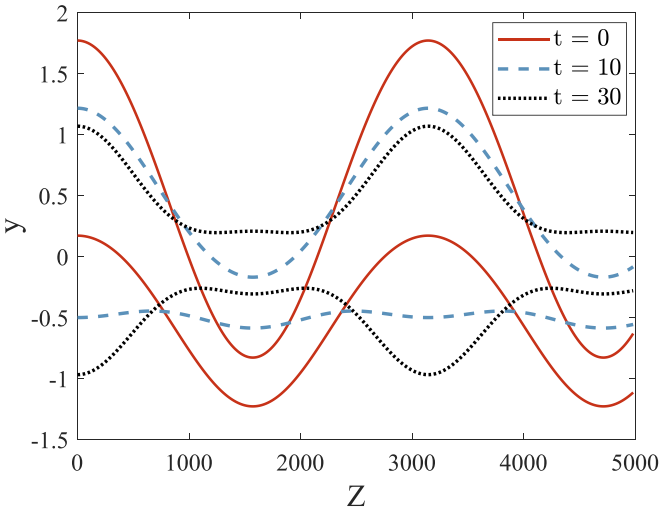

FIG. 14. Various schematic diagrams of nanostructures.

V. CONCLUSION

The paper investigates the nonlinear instability of three-layer nanoscale planar liquid sheets under dual-mode conditions. The second-order nonlinear analysis is conducted using the perturbation method. The findings reveal that second-order perturbations arising from the first-order varicose mode and first-order sinuous mode exhibit varicose characteristics, while the coupling of two modes generates sinuous mode second-order perturbations. However, the first-order sinuous mode and its second-order perturbations, as well as the second-order perturbations from the coupling of sinuous and varicose modes, make negligible contributions to the development of surface waves due to their continuous attenuation at a rapid rate. Consequently, the primary perturbations causing sheet rupture are those of the first-order varicose mode and its second-order perturbations.

The study also explores the effects of various parameters on the evolution of liquid sheet shape. A larger value of the dimensionless ratio of van der Waals force to surface tension α corresponds to a greater perturbation growth rate, as the promoting effect of van der Waals forces becomes more pronounced. Conversely, a higher viscosity ratio, β, results in a smaller growth rate due to the inhibitory influence of higher viscosity. Thus, higher α and lower β values lead to faster perturbation growth. Assuming the the liquid sheet will rupture, the liquid filaments will adopt an alternating pattern of main and satellite filaments. During surface wave development, although the initial amplitude of second-order perturbations is smaller, their growth rate is larger. Consequently, the proportion of second-order perturbations increases over time and may surpass that of first-order perturbations. The transmission of waves from first to second order dominates in second-order perturbations, ultimately playing a crucial role in the development of surface waves.

Furthermore, the potential application of the theory in nanothread manufacturing is investigated. Calculations are performed for liquid sheets of different thicknesses and various initial perturbation amplitudes. The cross-sectional area of both main and satellite liquid filaments is integrated using the Newton-Raphson method, and the ratio of their diameters, D_m/D_s, is determined. When ${}^1\tilde{\eta}_1/H < 0.1$, the diameter ratio remains stable at 1.91–1.94. The diameter of liquid filaments primarily depends on the sheet thickness. As ${}^1\tilde{\eta}_1/H$ increases, the diameter ratio D_m/D_s also increases, with a more pronounced trend when ${}^1\tilde{\eta}_1/H > 0.1$. In this case, the shorter rupture time prevents full development of second-order perturbations, allowing first-order perturbations to maintain a significant proportion. Consequently, the results differ from those obtained when second-order perturbations are fully developed.

Moreover, the influence of arbitrary initial perturbations is investigated. The results indicate that, within the range of the effective wave number k_e, the effect of arbitrary micro perturbations is negligible compared to the specific perturbation applied. This implies that specific perturbations can be employed to control surface wave development on the liquid sheet. Subsequently, the feasibility of fabricating nanofibers with special shapes using this approach is studied. The results demonstrate the formation of a wide variety of special shapes. These results can provide important guidance to achieve sophisticated nanostructures for functional devices in a single fiber or integrated fabrics.

However, the model in this paper and second-order nonlinear stability analysis still have certain limitations, such as the inability to accurately predict the rupture of the liquid sheet. Therefore, more work can be conducted in the future to precisely control the nanowire size and nanostructures within the fiber. This can be achieved by introducing stretching into the model, employing strong nonlinear models and solution methods, and considering non-Newtonian fluids, among other factors.

ACKNOWLEDGMENTS

This work was supported by the National Natural Science Foundation of China (Grants No. 12272026, No. 11927802, and No. U2341281) and the Navel University of Engineering (Grant No. 20225001200).

B.X. and Q.F. conceived the idea. X.Y. and B.X. performed the theoretical derivation. X.Y. conducted the result analysis and drafted the original manuscript. All authors discussed the results and revised the manuscript. All authors read and approved the final version of the manuscript.

DATA AVAILABILITY

The data that support the findings of this study are available from the contact authors upon reasonable request.

APPENDIX A

The results in Sec. III B are obtained by selecting the most advantageous wave number from linear analysis results as the dominant wave number for second-order analysis. In order to further validate the rationality of this selection, the second-order dispersion relation and the development of the liquid sheet with the maximum value of ω_2^v will be presented and compared with the case of maximum ω_1^v, to determine the validity of the aforementioned selection. Considering that the sinuous mode contributes almost nothing to the sheet breakup, we will only consider the varicose mode here.

Equation (59) provided the dimensionless calculation expression of the second-order growth rate Ω_2^v. The second-order dispersion relation can be directly plotted by using this formula, as shown in Fig. 15. Figure 15(a) shows the dispersion relation obtained by varying the ratio of van der Waals forces to interfacial tension α while keeping the viscosity ratio $\beta = 1$. Figure 15(b) shows the dispersion relation obtained by varying the viscosity ratio β while keeping the ratio of van der Waals forces to interfacial tension α fixed at $\alpha = 0.010$. From Fig. 15, it can be observed that the second-order dispersion relation has a high similarity to the first-order dispersion relation. The effects of different values of the α and different viscosity ratios are also consistent with those of the first-order dispersion relation. Moreover, the maximum growth rate of the second-order dispersion curve, $\Omega_{2,\max}^v$, is almost identical to that of the first-order dispersion curve, $\Omega_{1,\max}^v$. However, the dominant wave number when Ω_2^v is at its maximum is smaller than the dominant wave number when Ω_1^v is at its maximum. To further compare the magnitudes of $\Omega_{2,\max}^v$ and $\Omega_{1,\max}^v$, as well as the corresponding dominant wave number, Fig. 16 presents the curves of $\Omega_{2,\max}^v$ and $\Omega_{1,\max}^v$ with respect to the parameter α, as well as the curves of the dominant wave number with respect to α, considering three different viscosity ratios of $\beta = 1$, $\beta = 10$, and $\beta = 100$. From Fig. 16(a), it can be clearly seen that the dominant wave number $K_{1,\max}$ in the first-order case is twice that of the dominant wave

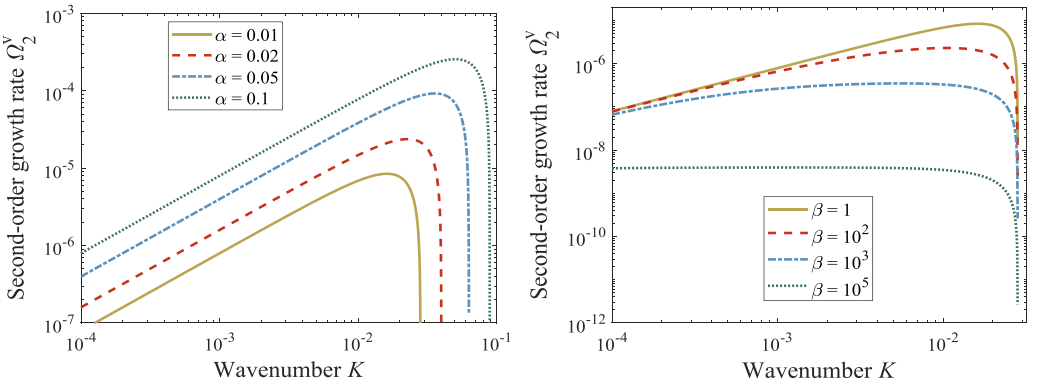

FIG. 15. Second-order dispersion relation of the varicose mode. (a) The effects of different ratios of van der Waals forces to interfacial tension α are considered with $\beta = 1$. (b) The effects of different viscosity ratios β are considered with $\alpha = 0.01$.

number $K_{2,\max}$ in the second-order case, and this conclusion holds for different viscosity ratios. Meanwhile, Fig. 16(b) shows that, when the values of α and the viscosity ratio β are the same, $\Omega^v_{1,\max}$ and $\Omega^v_{2,\max}$ are completely equal. Therefore, it is necessary to further supplement the specific shape of the surface wave on the liquid sheet in order to determine whether it is reasonable to choose $K_{1,\max}$ as the dominant wave number.

Figure 17(a) shows the temporal evolution of the liquid sheet shape when $K_{2,\max}$ is selected as the dominant wave number. In this case, the ratio of van der Waals forces to interfacial tension $\alpha = 0.010$, the viscosity ratio is $\beta = 1$, and the dimensionless initial disturbance in the first-order mode is ${}^{1,v}\tilde{\eta}_1^* = 0.1$. The amplitude of the disturbance is significantly smaller than the result shown in Fig. 5(a) when $K_{1,\max}$ is selected as the dominant wave number. This means that the disturbance develops more slowly when $K_{2,\max}$ is selected as the dominant wave number. Figure 17(b) presents a more intuitive comparison of the time required for sheet rupture by considering Ω_1^v and Ω_2^v as the primary growth rates, with two different viscosity ratios, i.e., $\beta = 1$ and $\beta = 100$, being investigated. As revealed by Fig. 9(b), taking Ω_1^v as the primary growth rate results in a shorter

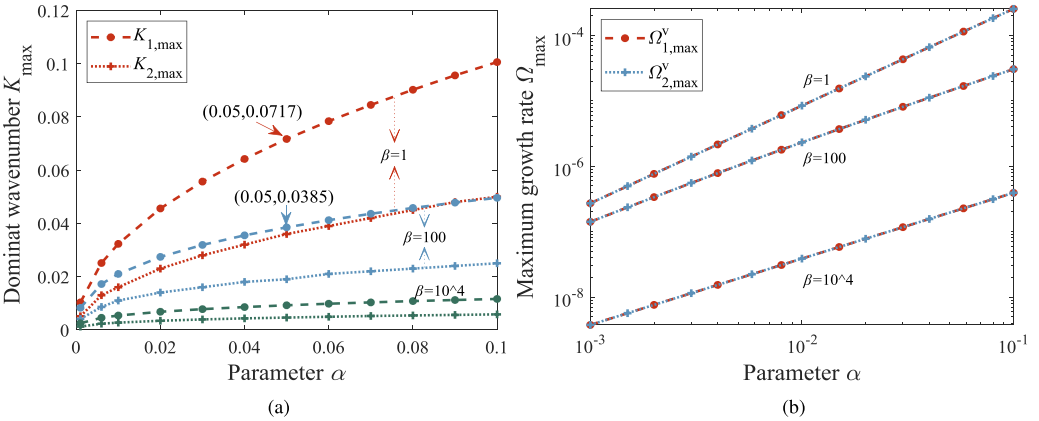

FIG. 16. Comparison of first and second-order results under different ratios of van der Waals forces to interfacial tension α and viscosity ratios β with the perturbation of varicose mode. (a) Dominant wave number. (b) Maximum growth rates.

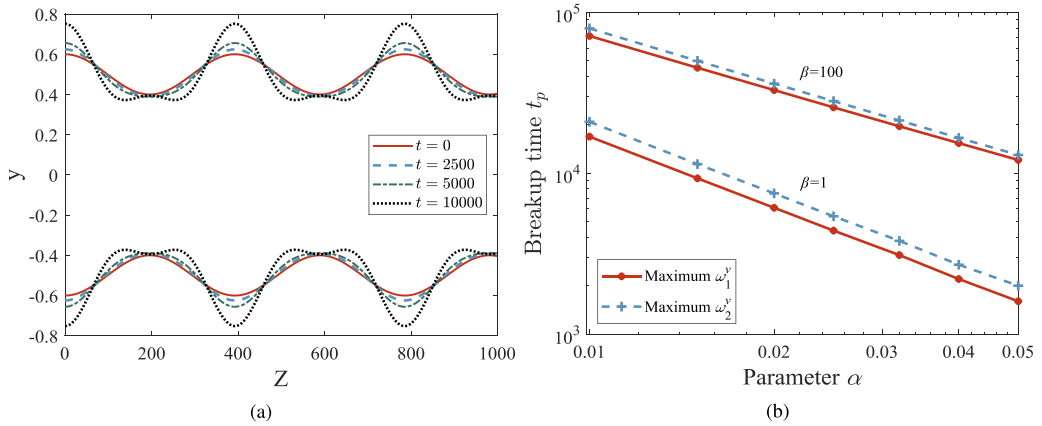

FIG. 17. Comparison between first and second-order results under varicose mode. (a) Development of the liquid sheet shape when taking the wave number corresponding to $\Omega^v_{2,\max}$ as the dominant one. The parameters are set as follows: $\alpha = 0.010$, ${}^1\tilde{\eta}_1^* = 0.1$, and $\beta = 1$. (b) Comparison of the time required for liquid sheet rupture when taking $K_{1,\max}$ and $K_{2,\max}$ as the dominant wave numbers. The dimensionless initial first-order perturbation is ${}^1\tilde{\eta}_1^* = 0.1$

period for sheet rupture, which holds true for different parameter values of α and distinct viscosity ratios. Therefore, it is demonstrated that it is reasonable to choose the most dominant wave number as the characteristic wave number for the second-order analysis based on the linear analysis results, because this is the case with the fastest disturbance development.

APPENDIX B

Detailed data on the diameter of the main and satellite nanowires are presented in Tables III and IV, respectively. By analyzing these data it can be inferred that, when the thickness is significantly larger than the disturbance, the diameter of the main liquid thread has little correlation with the initial disturbance amplitude. This phenomenon can be attributed to the fully developed second-order disturbance, which dominates under this circumstance. The diameter of the main liquid thread is predominantly determined by the surface wave wavelength, or the dominant wave number k. Notably, the dominant wave number is a function of the maximum growth rate, which is only dependent on the thickness when the physical properties are kept constant. Therefore, the adjustment of the thickness can effectively control the diameter of the main liquid thread.

TABLE III. The diameter of main fibers: D_m (nm).

	The sheet thickness H (nm)				
${}^1\tilde{\eta}_1$ (nm)	100	80	60	40	20
2	1471.2	1053.0	681.18	373.26	132.74
4	1471.3	1053.4	681.46	373.72	133.85
6	1471.8	1053.9	682.04	374.86	136.18
8	1472.4	1054.7	683.28	376.88	139.51
10	1473.5	1056.1	685.10	379.88	143.56

TABLE IV. The diameter of satellite fibers: D_s (nm).

	The sheet thickness H (nm)				
${}^1\tilde{\eta}_1$ (nm)	100	80	60	40	20
2	768.2	548.9	351.9	192.7	66.92
4	768.0	548.6	351.5	191.9	65.07
6	767.4	547.9	350.5	190.0	61.03
8	766.3	546.4	348.7	186.7	54.61
10	764.7	544.2	345.8	181.7	45.41

APPENDIX C

Here, we compare the liquid film profiles near rupture for two cases: (a) small thickness with large initial disturbance, and (b) large thickness with small initial disturbance. We also examine the relative contributions of the first-order and second-order disturbances. The two scenarios selected are $H = 20$ nm, $\eta_1 = 10$ nm for the small-thickness, large-disturbance case, and $H = 100$ nm, $\eta_1 = 2$ nm for the large-thickness, small-disturbance case.

The results near rupture are shown in Fig. 18. Figure 18(a) illustrates the small-thickness, large-disturbance case, where the amplitude of the first-order disturbance is significantly larger than that of the second-order disturbance. This is because the rupture time is short in this case, allowing insufficient time for the second-order disturbance to develop, resulting in a smaller amplitude. Consequently, the satellite thread diameter is relatively small, indicating a lower ratio of satellite to primary thread diameter. In contrast, for the large-thickness, small-disturbance case [Fig. 18(b)], the first-order disturbance amplitude is smaller than that of the second-order disturbance. The longer rupture time here allows sufficient development of the second-order disturbance, leading to a relatively larger satellite thread diameter and a higher ratio of satellite to primary thread diameter.

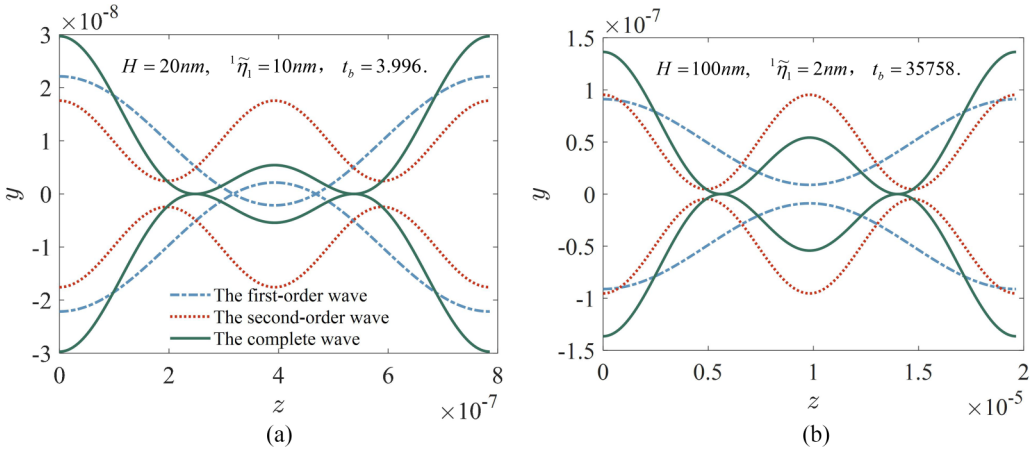

FIG. 18. Scenarios of a liquid film approaching rupture: (a) small thickness with large initial disturbance, (b) large thickness with small initial disturbance. Here, t_b denotes the time when rupture is imminent.

[1] A. Oron, S. H. Davis, and S. G. Bankoff, Long-scale evolution of thin liquid films, Rev. Mod. Phys. **69**, 931 (1997).
[2] J. B. Grotberg, Pulmonary flow and transport phenomena, Ann. Rev. Fluid Mech. **26**, 529 (1994).
[3] R. V. Craster and O. K. Matar, Dynamics and stability of thin liquid films, Rev. Mod. Phys. **81**, 1131 (2009).
[4] H. B. Squire, Investigation of the instability of a moving liquid film, Br. J. Appl. Phys. **4**, 167 (1953).
[5] W. W. Hagerty and J. F. Shea, A study of the stability of plane fluid sheets, J. Appl. Mech. **22**, 509 (1955).
[6] S. P. Lin, Stability of a viscous liquid curtain, J. Fluid Mech. **104**, 111 (1981).
[7] X. Li and R. S. Tankin, On the temporal instability of a two-dimensional viscous liquid sheet, J. Fluid Mech. **226**, 425 (1991).
[8] X. Li, Spatial instability of plane liquid sheets, Chem. Eng. Sci. **48**, 2973 (1993).
[9] D. R. Brown, A study of the behaviour of a thin sheet of moving liquid, J. Fluid Mech. **10**, 297 (1961).
[10] S. Mitra, X. Li, and M. Renksizbulut, On the breakup of viscous liquid sheets by dual-mode linear analysis, J. Propul. Power **17**, 728 (2001).
[11] H. R. Asare, R. Takahashi, and M. A. Hoffman, Liquid sheet jet experiments: Comparison with linear theory, J. Fluids Eng. **103**, 595 (1981).
[12] R. Dyson, J. Brander, C. Breward, and P. Howell, Long-wavelength stability of an unsupported multilayer liquid film falling under gravity, J. Eng. Math. **64**, 237 (2009).
[13] H.-y. Ye, L.-j. Yang, and Q.-f. Fu, Spatial instability of viscous double-layer liquid sheets, Phys. Fluids **28**, 102101 (2016).
[14] K. Matsuuchi, Instability of thin liquid sheet and its break-up, J. Phys. Soc. Jpn. **41**, 1410 (1976).
[15] C. J. Clark and N. Dombrowski, Aerodynamic instability and disintegration of inviscid liquid sheets, Proc. Math. Phys. Eng. Sci. **329**, 467 (1972).
[16] S. A. Jazayeri and X. Li, Nonlinear instability of plane liquid sheets, J. Fluid Mech. **406**, 281 (2000).
[17] L. J. Yang, C. Wang, Q. F. Fu, M. L. Du, and M. X. Tong, Weakly nonlinear instability of planar viscous sheets, J. Fluid Mech. **735**, 249 (2013).
[18] L. J. Yang, P. M. Chen, and C. Wang, Effect of gas velocity on the weakly nonlinear instability of a planar viscous sheet, Phys. Fluids **26**, 074106 (2014).
[19] C. Wang, L. J. Yang, and H. Y. Ye, Nonlinear dual-mode instability of planar liquid sheets, J. Fluid Mech. **778**, 621 (2015).
[20] S. Hart, G. Maskaly, B. Temelkuran, P. Prideaux, J. Joannopoulos, and Y. Fink, External reflection from omnidirectional dielectric mirror fibers, Science **296**, 510 (2002).
[21] K. Kuriki, O. Shapira, S. Hart, G. Benoit, Y. Kuriki, J. Viens, M. Bayindir, J. Joannopoulos, and Y. Fink, Hollow multilayer photonic bandgap fibers for nir applications, Opt. Express **12**, 1510 (2004).
[22] C. Dubois, C. Dubois, N. Guo, Y. Gao, A. Dupuis, F. Boismenu, S. Lacroix, and M. Skorobogatiy, Drawing of the hollow all-polymer Bragg fibers, Opt. Express **14**, 5838 (2006).
[23] A. F. Abouraddy, M. Bayindir, G. J. Benoit, S. D. Hart, K. Kuriki, N. D. Orf, O. Shapira, F. Sorin, B. Temelkuran, and Y. Fink, Towards multimaterial multifunctional fibres that see, hear, sense and communicate, Nat. Mater. **6**, 336 (2007).
[24] F. Sorin, A. F. Abouraddy, N. D. Orf, O. Shapira, J. Viens, J. Arnold, J. D. Joannopoulos, and Y. Fink, Multimaterial photodetecting fibers: a geometric and structural study, Adv. Mater. **19**, 3872 (2007).
[25] T. Nguyen-Dang, A. C. De Luca, W. Yan, Y. P. Qu, A. G. Page, M. Volpi, T. Das Gupta, S. P. Lacour, and F. Sorin, Controlled sub-micrometer hierarchical textures engineered in polymeric fibers and microchannels via thermal drawing, Adv. Funct. Mater. **27**, 1605935 (2017).
[26] D. S. Deng, J.-C. Nave, X. Liang, S. G. Johnson, and Y. Fink, Exploration of in-fiber nanostructures from capillary instability, Opt. Express **19**, 16273 (2011).
[27] X. Liang, D. S. Deng, J.-C. Nave, and S. G. Johnson, Linear stability analysis of capillary instabilities for concentric cylindrical shells, J. Fluid Mech. **683**, 235 (2011).
[28] B. R. Xu, S. Q. Ma, Y. Z. Xiang, J. Zhang, M. F. Zhu, L. Wei, G.-L. Tao, and D. S. Deng, In-fiber structured particles and filament arrays from the perspective of fluid instabilities, Adv. Fiber Mater. **2**, 1 (2020).

[29] D. S. Deng, N. Orf, A. Abouraddy, A. Stolyarov, J. Joannopoulos, H. Stone, and Y. Fink, In-fiber semiconductor filament arrays, Nano Lett. **8**, 4265 (2008).

[30] W. Esposito, L. Martin-Monier, P. L. Piveteau, B. R. Xu, D. S. Deng, and F. Sorin, Controlled filamentation instability as a scalable fabrication approach to flexible metamaterials, Nat. Commun. **13**, 6154 (2022).

[31] P.-G. de Gennes, F. Brochard-Wyart, and D. Quéré, *Capillarity and Wetting Phenomena* (Springer, New York, 2004).

[32] B. R. Xu, M. H. Li, F. Wang, S. G. Johnson, Y. Fink, and D. S. Deng, Filament formation via the instability of a stretching viscous sheet: Physical mechanism, linear theory, and fiber applications, Phys. Rev. Fluids **4**, 073902 (2019).

[33] B. R. Xu and D. S. Deng, Linear analysis of dewetting instability in multilayer planar sheets for composite nanostructures, Phys. Rev. Fluids **5**, 083904 (2020).

[34] A. Javadi, J. Eggers, D. Bonn, M. Habibi, and N. M. Ribe, Delayed capillary breakup of falling viscous jets, Phys. Rev. Lett. **110**, 144501 (2013).

[35] X. D. Liang, Modeling of fluids and waves with analytics and numerics, Ph.D. thesis, Massachusetts Institute of Technology, 2014 (unpublished).

[36] L. Rayleigh, On the instability of jets, Proc. London Math. Soc. **s1-10**, 4 (1878).

[37] L. J. Liu and L. J. Yang, Nonlinear wave evolution of shear-thinning carreau liquid sheets, J. Fluid Mech. **859**, 659 (2019).

[38] W. Yan, Y. P. Qu, T. Das-gupta, A. Darga, T. Nguyen-Dang, A. Page, M. Rossi, M. Ceriotti, and F. Sorin, Semiconducting nanowire-based optoelectronic fibers, Adv. Mater. **29**, 1700681 (2017).

[39] W. Yan, I. Richard, G. Kurtuldu, N. James, G. Schiavone, J. Squair, T. Nguyen-Dang, T. Das-gupta, Y. P. Qu, J. Cao, R. Ignatāns, S. Lacour, V. Tileli, G. Courtine, J. Löffler, and F. Sorin, Structured nanoscale metallic glass fibres with extreme aspect ratios, Nat. Nanotechnol. **15**, 875 (2020).